EPSC2018

TP8/OPS11/MD5/SB23 abstracts

EPSC Abstracts
Vol. 12, EPSC2018-48, 2018
European Planetary Science Congress 2018
© Author(s) 2018

Asthenospheres of the rocky planets and the Moon: a reason of their origin

G. Kochemasov, IGEM of the Russian Academy of Sciences, 35 Staromonetny, 119017 Moscow, RF, kochem.36@mail.ru

The Earth-Moon system widens with time that is increases its angular momentum. A natural reaction to this is slowing of the system' both bodies rotation diminishing the angular momentum (action – anti-action). The diminishing momenta are compensated by melting and uplifting to the surface of dense basaltic material [3-5]. But on the Moon this happens early (3-4.5 billion years ago) because of diminished inertia of the small satellite mass. Essentially "postponed" by time this process was on much more massive and inert Earth (the Jurassic-Cenozoic). Earth is 81 times more massive than its satellite. (3-4.5 b.y.) : 81 = 37-55 mln. y. According to these calculations the "peak" of the "basaltic" reaction of Earth, filling in oceanic basins gets into the boundary of the Mz-Cz. One more peculiarity of basaltic infillings of terrestrial oceans and lunar basins is in relatively high Fe content of the latter. This peculiarity speaks on smaller temperatures of basalt melting out of the lunar mantle and the higher their density. This correlates with a notion of relatively low temperatures in the mantle at the initial periods of transformation of the mechanical energy of moving to the heat energy for the mantle melting – creating asthenosphere.

. Despite of enormous age differences between lunar and terrestrial basaltic covers (billions of years!) some common chemical shift of their compositions is notable and significant. Let us compare Procellarum Basin and Pacific Ocean basalts. The oldest parts of their covers occur in the W of Procellarum (KREEP) and SW of the Pacific (Ontong Java Plateau – the largest LIP of Earth). Potassium, phosphorus, rare earths, thorium enrich the older lunar KREEP basalts. The older terrestrial oceanic Ontong Java basalts (Cretaceous age-about 122 mln. y) also show "KREEP trend". They belong to E-MORBs and have elevated values of potassium, lithium, chlorine, REE, thorium. Elevated Fe/Mg (and siderofile platinum group elements) also is in Ontong Java basalts [1, 2]. All these chemical peculiarities distinguish them from the younger N-MORBs of other parts of the Pacific Ocean (EPR, for example). As all considered basalt melts of both bodies originate in asthenopheres, the older parts of these melts derive from relatively earlier "cool" asthenosphere. It means that only easily melted alkali and iron rich parts were involved in the process. Later on, significantly heated asthenospheres produced enormous volumes of chemically different (less alkaline and more magnesian) basalts. In this sense, rather impressive is a comparison of the lunar iron and thorium geochemical maps stressing coincidence of their anomalies in the Procellarum KREEP terrain area (Fig. 1, 2).

The considered time development of basaltic magmatism could be paralleled with the development of alkaline terrestrial magmatism [6]. Its earlier older parts often are more alkaline than later Cenozoic parts. Famous large agpaitic massifs are mainly Proterozoic-Paleozoic in age. Again, early "cold" asthenosphere produces more easily melted relatively small alkaline parts than the later "hot" asthenosphere making large volumes of deeply melted more magnesian less alkaline ones.

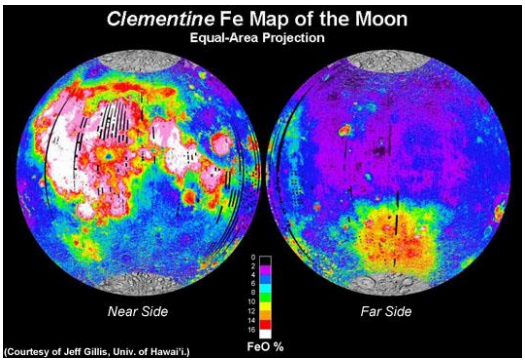

1

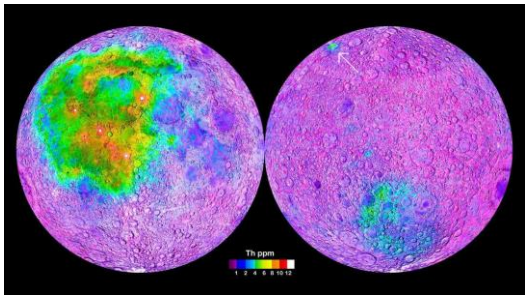

2

Mars is intermediate by mass between Earth and the Moon. It is ten times less massive than Earth and 11 times more massive than the Moon. Moving in the wider orbit with its own peculiarities, small Mars, nevertheless, also fills in its dichotomous Northern Basin (Vastitas Borealis) by relatively ferruginous basalts. Beginning of the effusions is considered, by impact (?) crater counts, to be in the end of the Hesperian, that is about 3 b.y. ago. The last ages of crater infillings in the giant volcanoes are determined as 3 b.- 500-200 m. y.[7-9]. Counting age of massive effusions by the mass relations of Earth (Moon) and Mars (understanding difference in orbits influencing warming mantle and melting basalts) one gets ages 400-270 m. y. The rejuvenation of melting out intervals and their widening in Mars is evident, what resembles terrestrial processes.

According to sequence of masses and inertia of above three celestial bodies (not considering difference of their orbits) their planetary basaltic "explosions" form up a regular age row – from the oldest of some billion years to the Mz-Cz. The massive Venus also is regularly inscribed in this row with its vast Mg-rich basaltic cover. Giving up a little to the Earth by mass (but superior to it by the frequency of orbiting), it gives up a little to Earth in age of the basaltic "explosion". Counting impact (?) craters gives age about 500 mln.y. It is older than calculated (4.5-3 b.y.: 66= 68-45 mln.y.) but is not absolutely determined – the "explosion" could last some prolonged time.

Two inner planets – Venus and Mercury are united by big orbiting frequencies, slow rotations, abundant degasation (atmosphere is preserved on Venus and is "swept" away on Mercury), and abundant Mg-rich magmatism.

So, the terrestrial group planets and the Moon have various masses and a common significant geomorphologic peculiarity: their negative surface forms – depressions of various scales (oceans, basins, seas) are filled with dark dense basaltic material. It is explained by that the loss by bodies of rotation rate, that means angular momentum, must be compensated by transfer to surface of relatively dense basaltic material. To prepare basaltic melts, in the mantle depths temperature must be raised to a certain level, and in bodies significantly differing by mass and rather impoverished in heat-generating radioactive elements. A plausible process for this is transition of the mechanical energy of orbital movement into the heat energy. This process is connected with a mass or inertia bodies. If the mantle of the smallest body – the Moon is warmed up quickly and the absolute ages of the surface basalts are 3-4.5 b. y. , then oceans of the massive and inert Earth are filled with basalts aged some tens of million years and even modern. Other three planets with intermediate masses show intermediate ages of basaltic "explosions".

Wide basaltic covers are characteristic for the rocky planets and the Moon. However, ages of basaltic effusions are significantly different. Small Moon develops asthenosphere for making melts very earlier- 3-4 billion y. ago. 81 times more massive Earth develops its asthenosphere much later- in the MZ-Cz. These age differences are proportional to their masses. In both bodies the earlier basaltic melts are richer in alkalies and iron reflecting a "cool" state of the earlier asthenospheres. Later, the "warmer" mature ashtenospheres produce large volumes of less alkalic more magnesian basalts.

References:

1. Ely J.C. and Neal C.R. Using platinum-group elements to investigate the origin of the Ontong Java Plateau, SW Pacific // Chemical Geology, v. 196, 2003, 235-257. **2**. Hiesinger H., and J.W. Head III. (2016) Ages of Oceanus Procellarum basalts and other nearside mare basalts //Workshop on New Views of the Moon II, 2016, abs.8030. **3**. Kochemasov G.G. (2014) Earth and Moon: similar structures – common origin // NCGT Journal, 2014, v. 2, # 2, 28-38. **4.** Kochemasov G.G. (2015) A lunar "mould" of the Earth's tectonics: four terrestrial Oceans and four lunar Basins are derivative of one wave tectonic process // NCGT Journal, v. 3, # 1, 2015, 29-33. **5.** Kochemasov G.G. New planetology and geology: tectonic identity and principal difference of terrestrial oceans and lunar basins // New Concepts in Global Tectonics (NCGT) Journal, 2017, V. 5, # 1, p 131-133. **6.** Kogarko L.N. and Khain V.E. Alkaline magmatism in the Earth's history: geodynamical interpretation // Doklady of the Academy of Sciences. 2001. vol. 377 Iss. 5 pp. 677-679 (in Russian). **7.** Martel, Linda M.V. (2005-01-31). "Recent Activity on Mars; Fire and Ice". Planetary Science Research Discoveries. Retrieved 2006-07-11. **8.** Neukum G. et al. Surface age of martian shield volcanoes and channels // Abstracts X Lunar and Planetary Science Conference, March 19-23 1979, part 2, p. 907-909. **9.** Neukum G., et al. (2004) "Recent and Episodic Volcanic and Glacial Activity on Mars Revealed by the High Resolution Stereo Camera". Nature, v. 432, 971- 979. doi: 10.1038/nature03231. PMID 15616551..

EPSC Abstracts
Vol. 12, EPSC2018-54, 2018
European Planetary Science Congress 2018
© Author(s) 2018

Analyzing pit chains in Iceland to constrain regolith thickness on Enceladus

Jennifer L. Whitten, and Emily S. Martin
(1) Smithsonian Institution, National Air and Space Museum, Center for Earth and Planetary Studies, Washington DC, USA, (whittenj@si.edu)

1. Introduction

The surface of Enceladus is mantled with a layer of regolith hypothesized to be sourced by both impact cratering and fallback from the south polar plumes [1]. This layer of unconsolidated regolith may contribute to muting surface morphology, erasing small craters [2], and insulating the surface [3–6]. In particular, the insulating effects of such a regolith layer would raise the effective surface temperature and have a significant influence on thermal models of Enceladus [6]. Therefore, it is important to understand the distribution and depth of regolith on Enceladus to better constrain thermal models, plume activity, and perhaps the longevity of the south polar plumes and a global subsurface ocean.

1.1 Measuring Regolith

The regolith distribution and thickness can be assessed on Enceladus using pit chains. Pit chains are linear assemblages of circular to elliptical depressions that form in regolith and are observed on planetary bodies across the solar system [7], including Earth. There are a variety of processes that may form pit chains [8], but pit chains on Enceladus typically form where regolith overlies extension fractures [8–11].

Previous work [12] has shown that pit chains (Fig. 1) can be used to measure local regolith depths, adopting a method established by [8] for terrestrial planetary bodies. The assumption of this technique is that a pit reaches the base of the regolith layer, thus pit depth is a proxy for regolith depth. Since the pit may not necessarily penetrate the entire regolith layer the measured pit depth is a minimum estimate of regolith depth. Orbital images can be used to measure the depth of individual pits by assuming each pit is a cone and its depth can be calculated based on geometric relationships [8].

Here, we ground truth this proxy by making measurements and observations of terrestrial pit chains in Iceland to determine (1) if the geometric relationships [8] accurately predict pit depth and (2) verifying whether the depth of the soil is equivalent to the depth of the pit. Measuring the distribution of regolith thickness across Enceladus using pit chains is a necessary first step in separating the contribution of plume materials from impact cratering in regolith production, and ultimately understanding the persistence of plume activity.

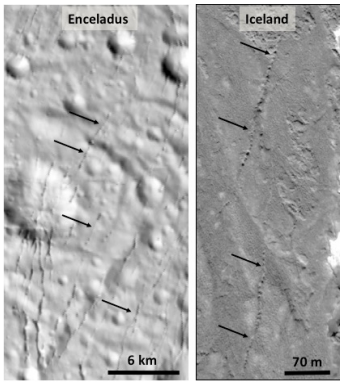

Figure 1: Pit chains on Enceladus (left) and in Iceland (right).

2. Methods

On Earth, pit chains have been identified in various locations [e.g. 13] and those around the Krafla volcano in northern Iceland serve as a representative analog for pit chains on Enceladus [10, 11] (Fig. 1). As extension cracks on Enceladus dilate, regolith drains into the existing void forming pits along the trace of the crack. Similarly, in Iceland cracks form in the underlying basalt, and the overlying soil drains into the underlying crack [10]. The cold icy crust of Enceladus behaves in much the same way as the basaltic bedrock in Iceland, making these basalts an ideal material analog for the water ice and snow-like regolith across Enceladus. The ice sheets across the Earth are too warm and behave too ductility to be

appropriate analogs for pit chain formation on Enceladus.

In August, 2017 and May, 2018, we traveled to northern Iceland, just north of the Krafla volcano, to make morphometric measurements of individual pits within pit chains. Pit diameter was measured along strike and perpendicular to strike to characterize potential ellipticity [i.e. 8]. Pit depth was measured using a laser ranger instrument, and images were obtained to generate digital elevation models of pits to assess the validity of using a cone as a representation of pit shape.

In addition, soil depth was measured with both a ground penetrating radar (GPR) system and a tiling probe to more completely constrain the soil depth measurements. We used a GSSI SIR-3000 control unit with a 200 and 400 MHz antenna to collect GPR tracts adjacent to several of the measured pits (both sub-parallel and perpendicular tracks). The 200 and 400 MHz antennas were selected because they would be sensitive to the estimated regolith-bedrock boundary, rather than smaller-scale variations within the regolith like layering, rocks, or other debris.

3. Results

Data were collected from pits based on the preservation of their walls and floor to ensure accurate diameter measurements. As a result, all of the pits measured in Iceland were located the tips of their fractures where the least amount of extension has occurred, rather than in the central, or widest, portion of the fracture. Due to the similar location of measured Icelandic pits along the fractures, all of the pits are of approximately the same dimeter, ~5–8 m (Fig. 2). Comparing the ratio of pit depth and dimeter values with those measured for pits on Enceladus [12] and other planets (Mars [8], Earth [10]), Icelandic pits from this study are deeper than calculated on Enceladus using the proxy. The Icelandic pits depth to diameter ratios plot substantially close to a 1:1 line compared with the other planetary bodies (Fig. 2). While the Iceland pits are slightly more circular, these features are elongated perpendicular to the fracture trace. Additional data are required of both smaller and lager pits to more thoroughly test whether they are consistently deeper, or if the method for inferring depth of Enceladus pits needs refinement. Differences that are visible in the preliminary data may also be due variations in the material properties of basalt regolith and Enceladus's 'snow' regolith.

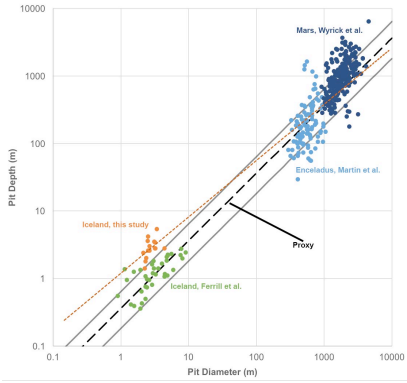

Figure 2: Measured (orange, green) and calculated (dark and light blue) [8] relationships between pit chain pit diameter and pit depth.

4. Summary

We will present processed GPR data of regolith depths near the 15 measured pits and compare Icelandic results with those inferred for Enceladus. We are returning to Iceland May of 2018 to complete data collection in the same lava fields around the Krafla volcano in northern Iceland. Additional measurements will be made in deltaic deposits along the northern coast of Iceland to characterize how the material properties of the regolith might influence the shape of a pit.

Acknowledgements

The authors would like to acknowledge the Smithsonian for funding this research through the Scholarly Studies Awards Program and generous individual donations.

References

[1] Kempf, S. et al., Icarus, 206, 446–457, 2010. [2] Kirchoff, M. R. & Schenk, P., Icarus, 202, 656–668, 2009. [3] Passey, Q. R. & Shoemaker, E. M., in Satellites of Jupiter, pp. 379–434, 1982. [4] Squyres, S. W. et al. Icarus, 53, 319–411, 1983. [5] Passey Q. R., Icarus, 53, 105–120, 1983. [6] Bland, M.T. et al., GRL, 39, L17204, 2012. [7] Wyrick, D.Y. et al., LPSC XXXXI, abs #1413, 2010. [8] Wyrick, D.Y. et al., JGR, 109, E06005, 2004. [9] Ferrill, D.A. et al., GSA Today, 14, 4–12, 2004. [10] Ferrill, D.A. et al., Lithosphere, 3, 133–142, 2011. [11] Martin, E.S. et al., Icarus, 294, 209–217, 2017. [12] Martin, E.S. & Kattenhorn, S.A. et al., LPSC XXXXIV, abs #204, 2013. [13] Okubo, C.H. & Martel, S.J., J. Volc. Geotherm. Res., 86, 1–18, 1998.

EPSC Abstracts
Vol. 12, EPSC2018-106, 2018
European Planetary Science Congress 2018
© Author(s) 2018

Evolution of the lunar basaltic magmatism: Basins and Marea covers

G. Kochemasov, the Russian Academy of Sciences, 35 Staromonetny, 119017 Moscow, RF, kochem.36@mail.ru

Several enigmatic structural and petrologic features of the Moon are widely discussed: origin and global spreading of the high-Ti lunar basalts, mascons, swirls. The Moon moves away from Earth. Loosing its angular momentum due to slowing rotation a necessary compensation is fulfilled by sending dense materials into the crust (Fig. 1, 2). Varying density basalt flows (high, low, very low-Ti) reflect various stages of the slowing rotation process. Various contents of dense mineral component – ilmenite in basalts means various densities of the rock. Iron in basalts can be in less dense dark minerals and denser ilmenite thus influencing overall basalt densities corresponding to requirements of "healing" diminishing angular momentum.

Spectral mapping of basalt types [8] indicate that for large parts of Oceanus Procellarum younger basalts are more titanium rich than the older basalts, thus somewhat reversing the trend found in the returned samples [6]. In some smaller basins spectral mapping also shows titanium richer basalts being older than titanium pure ones [5]. Thus, one may conclude that decreasing rotation rate of the Moon was not smooth but rather uneven.

The deepest SPA Basin must be filled with denser rocks than the shallower Procellarum Ocean filled with basalts and Ti basalts. The Clementine spectral data show presence of orthopyroxene and absence of plagioclase [8] favoring some dense ultrabasic rocks. An obvious tendency to approach this type of rock would be to observe it in the Luna 24 samples from also very deep (up to 4. 5 km) Mare Crisium. In fragments there prevail pyroxene and VLT-ferrobasalts (Mg-poor). Unusual melt matrix breccia with globules and crystals of Fe metal were also found [1]. Among glass droplets there 40-54 % are irons. Nearly half of the black and brown droplets have either vesicles or iron droplet trains or both [1, 2]. A significant portion of Mg enriched fragments in the Luna 24 soil is also observed.

The lunar global magnetic map (Fig.3) favours a conclusion about some important Fe metal admixture increasing not only magnetism but also overall rock density of the deepest Basins and Mares. An association of Mg-pyroxene enstatite with Fe-Ni metal is well known in cosmic materials (for an example, E-chondrites). On the Moon enigmatic but characteristic swirls with high albedo, elevated magnetism and diffused boundaries could be presented by this type of high-Mg (light in color) with Fe metal rock. The SPA Basin is one of the enriched with swirls relatively magnetic areas (Fig. 3) [3]. In the Reiner Gamma swirl area some small rifts are detectable.

Another not less important repairing instrument for the diminishing momentum is an introduction into the crust additional dense masses – mascons. Their bodies are rather typical and characteristic in the lunar crust. An important role of dense minerals (ilmenite, native Fe) in basaltic-UB covers in the lunar crust witnesses a compensating role of these effusions for loosing angular momentum of moving off satellite. Mascons appear in the crust for the same reason.

In summary, three enigmatic structural-petrologic phenomena are united by one general purpose – to heal the lost angular momentum. For the same purpose slowing rotation and loosing angular momentum much more massive and inert Earth introduces profuse basaltic masses mainly later, in PZ-Mz-Cz. Partial melting of the mantles of such different in masses bodies raises a long standing question of energy origin for such grandiose events.

Coming back to the SPA Basin, one should mention that presumed sizable concentrations of the metal iron in its bottom cover could be considered as an important source of this easily recovered (separated) material. Iron is important for the future construction works on the lunar surface and outside of it (near and far cosmos).

Despite of enormous age differences between lunar and terrestrial basaltic covers (billions of years!) some common chemical shift of their compositions is notable and significant. Let us compare Procellarum Basin and Pacific Ocean basalts. The oldest parts of their covers occur in the W of Procellarum (KREEP) and SW of the Pacific (Ontong Java Plateau – the largest LIP of Earth). Potassium, phosphorus, rare earths, thorium enrich the older lunar KREEP basalts. The older terrestrial oceanic Ontong Java basalts (Cretaceous age-about 122 mln. y) also show "KREEP trend". They belong to E-MORBs and have elevated values of potassium, lithium, chlorine,

REE, thorium. Elevated Fe/Mg (and siderofile platinum group elements) also is in Ontong Java basalts [4]. All these chemical peculiarities distinguish them from the younger N-MORBs of other parts of the Pacific Ocean (EPR, for example). As all considered basalt melts of both bodies originate in asthenopheres, the older parts of these melts derive from relatively earlier "cool" asthenosphere. It means that only easily melted alkali and iron rich parts were involved in the process. Later on, significantly heated asthenospheres produced enormous volumes of chemically different (less alkaline and more magnesian) basalts. In this sense, rather impressive is a comparison of the lunar iron and thorium geochemical maps stressing coincidence of their anomalies in the Procellarum KREEP terrain area (Fig. 1, 2).

References:

[1] Basu A.et al.(1977) Conference on Luna 24, Houston, LPI Contribution 304, p. 14-17. **[2]** Basu A. et al. (1977) the same, p. 18-21. **[3]** Denevi B.W. et al (2016) Icarus, v, 273, 15 July 2016, 53-67. doi.10.1016/j.icarus.2016.01.017. **[4]** Ely J.C. and Neal C.R. (2003) Using platinum-group elements to investigate the origin of the Ontong Java Plateau, SW Pacific // Chemical Geology, v. 196, 235-25.

[5] Hiesinger H. et al. (2000) J.Geoph.Res., 2000, v.185, #E12, 29239-275. **[6]** Hiesinger H. and J.W. Head III. (2016) Workshop on New Views of the Moon II, abs.8030. **[7]** Pieters C.M. (1978) Proc. Lunar Planet. Sci. Conf., 9th, 1978, 2825-2849. **[8]** Pieters C.M. (1997) Annales Geophysicae, Suppl. III to v. 15, p.792.

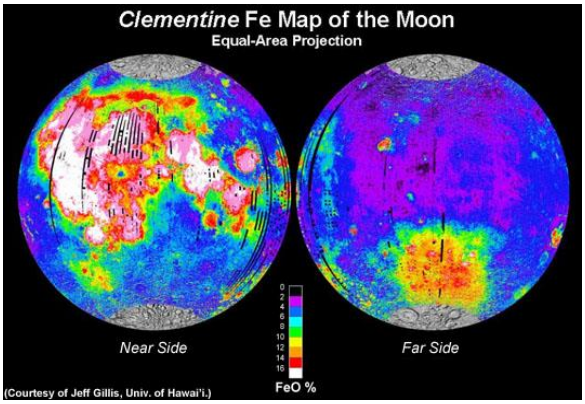

FIG. 1. LUNAR FE

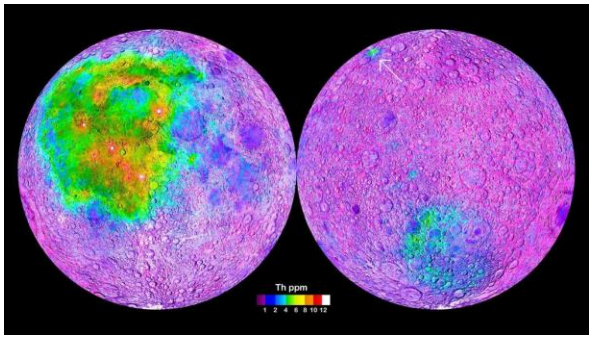

FIG. 2. LUNAR TH

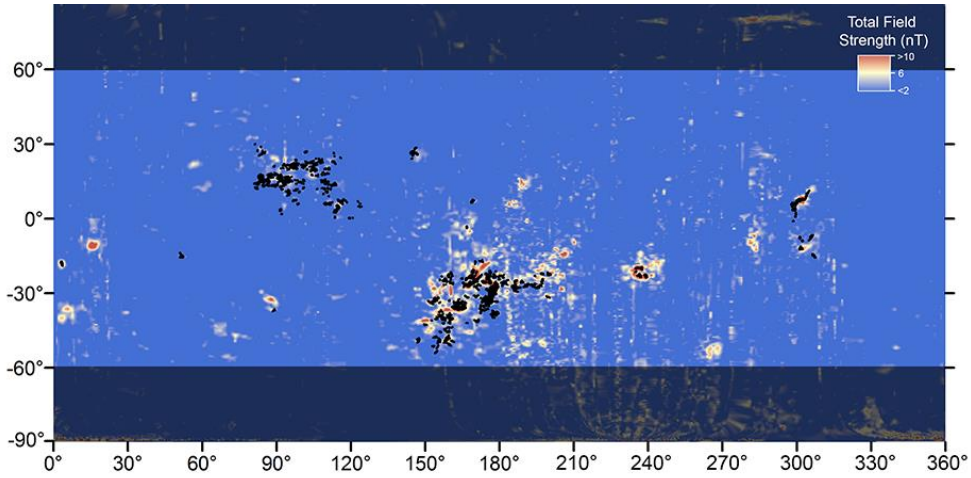

FIG. 3. LUNAR MAGNETISM [3]

EPSC Abstracts
Vol. 12, EPSC2018-112-2, 2018
European Planetary Science Congress 2018
© Author(s) 2018

Possible Subsurface Sediment Mobilization and Release of Volatiles in Southern Chryse Planitia, Mars

Petr Brož[(1)], Ernst Hauber[(2)], and Ilse van de Burgt[(2,3)]
[(1)] Institute of Geophysics, Czech Academy of Science, Czech Republic (petr.broz@ig.cas.cz), [(2)] Institute of Planetary Research, DLR, Berlin, Germany, [(3)] Utrecht University, The Netherlands.

Abstract

Here we present the results of our mapping of a large field of cones and pie-like features in the Chryse Planitia area on Mars, which have been previously described as mud volcanoes [1]. Our aim was to determine the full extent of this field and perform a comprehensive morphological, morphometrical, and spatial analysis of the landforms. We mapped a total of 1313 objects and distinguished five different morphological classes. The spatial distribution of the features is clustered and anticorrelated to the highlands, favoring a sedimentary origin.

1. Introduction

Ever since the presence of methane in the Martian atmosphere was first reported [2,3], mud volcanism was hypothesized to be a possible release mechanism [4], and various mud volcano fields have been tentatively identified [1]. It is difficult, however, to define diagnostic morphological properties of mud volcanism in remote sensing data, and some of the reported mud volcanoes have alternatively been interpreted as igneous volcanoes [5,6]. In this study, we test the hypothesis by Komatsu and colleagues [1] that small cone- or pie-shaped landforms in Chryse Planitia are mud volcanoes (as the use of the term "mud volcanism" has far-reaching implications [7-8], we prefer to follow a conservative approach and use the more generic term "subsurface sediment mobilization" [9]).

Our study area (8°N to 31°N/315°E to 330°E) is located near the southern boundary of Chryse Planitia at the terminations of the large outflow channels such as Ares, Simud, and Tiu Valles. Ancient highlands are eroded into streamlined "islands", and the former floor of the channels has been resurfaced and forms a relatively flat plain formed by flood deposits and possibly volcanics that slopes very gently towards north (<0.25°). These inter-island plains were mapped as Late Hesperian units HCc_3 and HCc_4 and Early Amazonian unit ABVm [10].

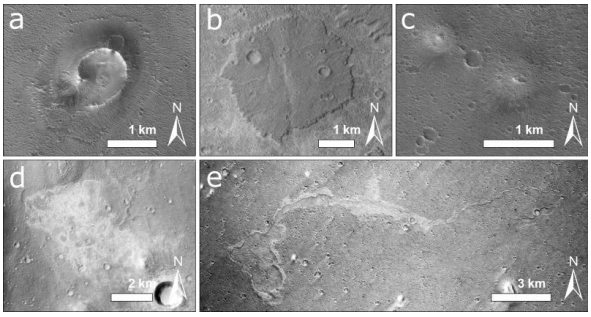

Figure 1: Five types of landforms that may be the surface manifestations of subsurface sediment mobilization. A) type 1, cones; (image: HiRISE); B) type 2, pies (image: CTX); C) type 3, domes (CTX); D) type 4, irregular pies (CTX). (e) type 5, [channelized] flow-likefeatures (CTX). Types 1-3 were already described by [1].

2. Data and methods

Several datasets were used for our morphological interpretations in the Chryse Planitia area: CTX (~5-6 m/pixel, [11]), HiRISE (~0.3 m/pixel, [12]), THEMIS daytime infrared (~100 m/pixel, [13]), and HRSC anaglyph images and Digital Elevation Models (~12.5 m/pixel [14]). Mapping was performed in a GIS (Geo-graphic Information System) environment and units and objects were demarkated as polygons, polylines and shape points. We mapped highlands, craters, ejecta blankets, possibly extrusive features, fractures, and wrinkle ridges. Spatial investigations of mapped objects include nearest neighbor analysis, rectangle analysis, circularity calculations and orientation analysis.

3. Results

Three types of landforms possibly indicative of extrusive processes in the study area were previously described [1]: type 1 (steep-sided cones; Fig. 1a),

type 2 (nearly flat, or pie-like, structures; Fig. 1b), and type 3 (nearly circular, dome-shaped features; Fig. 1c). We introduce two additional types: Type 4 (Fig. 1d), is characterized by a sheet-like appearance with irregular plan shape and lobate margins. Objects of this type are nearly flat (almost no topographical expression) and typically larger than 1 km in diameter, similar to type 2 features. Their surfaces are distinctively different from surrounding material, as they seem to exist of two different morphologies: light, smooth material, and dark, fractured material. In several areas these features can be observed in association with the other types suggesting that there may be a genetic link. Type 5 displays a flow-like appearance which is commonly associated with channels (Fig. 1e). The spatial distribution of the possibly extrusive features appears to be anticorrelated to the highlands (Fig. 2), in other words they only occur on the level plains between the erosional remnants of the ancient highland material. Nearest neighbour analysis shows a less than 1% likelihood that the spatial distribution could be random, i.e. the features are clustered. The different types appear in NEE-SWW oriented bands.

The minimum bounding geometry tool of ArcMap gives the length of the longer side of an enveloping rectangle around the polygons, and is here used as a proxy for the orientation of the extrusive features. We obtain a preferred E-W orientation, ranging from 65° to 115° (clockwise from North), with a mean orientation of 88°. Fractures appear mainly in patterns that are oriented parallel to the flow direction in the outflow channels, and their distribution is also anticorrelated to the highlands. The most densely populated fracture areas are observed in the northern (i.e. distal with respect to the outflow channel terminations) parts of the study area, without a clear correlation to the location of the conical features. Further up-stream (proximal), the fractures display more transverse orientations.

4. Conclusions

The spatial distribution of the mapped features, which are excusively located in the sedimentary plains between the erosional remnants of the ancient highlands (see Figure 2), suggests a formation mechanism that is linked to a relatively shallow source beneath or within the sediments. Igneous volcanoes fed from deep sources (e.g., distributed in monogenetic volcanic fields), on the other and, would be expected to be distributed on both the plains and the highlands. Our observations hence support previous conclusions [1] that an igneous origin is less likely than a sedimentary volcanic origin. Such conclusion is further supported by evidences of flow-like features caused by the movement of low viscous material, possibly a mixture of water with sediments.

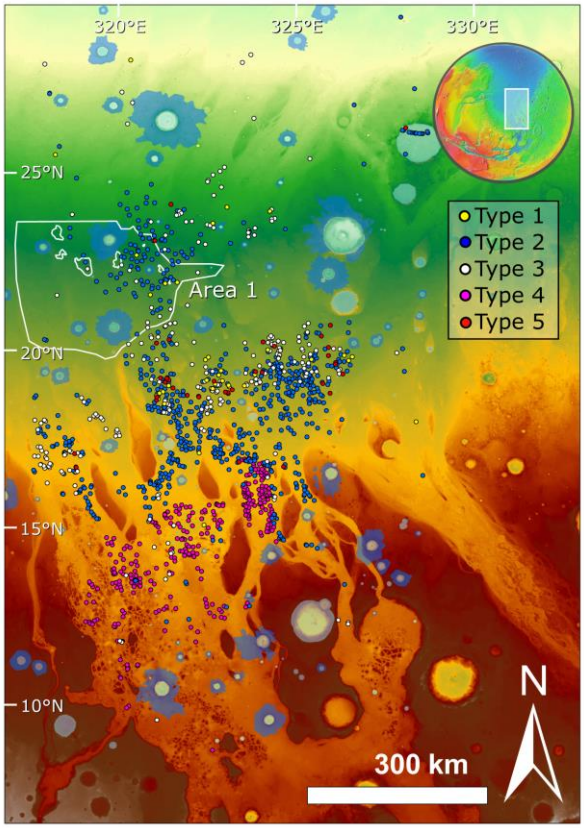

Figure 2: Overview of the mapped landforms on a HRSC DEM basemap. Yellow symbols: type 1 (cones), blue: type 2 (pie-like features); white: type 3 (domes); purple: type 4 (irregular sheet-like features); red: type 5 (large flows). The blue polygons around the impact craters mark the position of rampart ejecta.

5. References

[1] Komatsu et al. (2016) Icarus, 268. [2] Formisano et al. (2004) Science, 306. [3] Mumma et al. (2004) BAAS, 36. [4] Oehler and Etiope (2017) Astrobiology, 17. [5] Brož et al. (2013) JGR, 118. [6] Brož et al. (2017) EPSL, 473. [7] Kopf, A.J. (2002) Rev. Geophys., 40. [8] Mazzini and Etiope (2017) Earth-Sci. Rev., 168. [9] Van Rensbergen et al. (2003) Geol. Soc. Spec. Publ., 216. [10] Tanaka et al. (2005) USGS Sci. Inv. Map 2888. [11] Malin et al. (2007) JGR, 112, E05S04. [12] McEwen et al. (2007) JGR, 112, E05S02. [13] Christensen et al. (2004) SSR, 110. [14] Gwinner et al. (2016) PSS, 126. [15] Werner, S.C. et al. (2014) Science, 343.

EPSC Abstracts
Vol. 12, EPSC2018-193, 2018
European Planetary Science Congress 2018
© Author(s) 2018

How to Measure Io's Lava Eruption Temperatures with a Novel Infrared Detector and Readout Circuit

Ashley Gerard Davies (1), Alexander Soibel (1), David Z. Ting (1), William Johnson (1), Paul Hayne (2), Sarath D. Gunapala (1) and Megan Blackwell (3).
(1) Jet Propulsion Laboratory-California Institute of Technology, CA, USA, (2) University of Colorado Boulder, USA (3) Massachusetts Institute of Technology-Lincoln Laboratory, MA, USA. (Email: Ashley.Davies@jpl.nasa.gov)

1. Introduction

In the wake of NASA's *Galileo* mission to the Jovian system, perhaps the most important question that remains from the detailed investigation of Io concerns the composition of Io's dominant erupting lavas [1,2]. Measuring eruption temperature would help constrain lava composition, but this measurement is technically challenging using remote sensing, even though Io has hundreds of currently active volcanoes [3,4]. Io's widespread, extreme level of volcanic activity is the result of tidal heating [5], the result of an orbital resonance between Io, Europa and Ganymede. Internal heating and volcanic advection result from a complex interplay of processes dependent on internal viscosity and variability of viscosity, and therefore on composition and temperature. The mapping of eruption temperatures across Io may reveal spatial variations in heat production through tidal dissipation and suggest lateral variations in melt fraction [6].

Only certain styles of volcanic activity are suitable for determining eruption temperature remotely, those where thermal emission is from a restricted range of surface temperatures close to eruption temperature and filling an area large enough to be detected [2]. Such desirable processes include large lava fountains; smaller lava fountains common in active lava lakes; lava tube skylights; and transient but powerful explosive events [7].

Problems that must be overcome to obtain usable data are: (1) the rapid cooling of the lava between data acquisitions at different wavelengths; (2) the often unknown magnitude of thermal emission (see Figure 1) at any given time, which has often led to detector saturation; and (3) thermal emission changing on a shorter timescale than the observation integration time – newly exposed lava cools extremely fast from eruption temperature [2]. We can overcome these problems by using the HOT-BIRD detector and a novel, advanced digital readout circuit (D-ROIC) which saturates only under such extreme conditions that they are unlikely to be encountered on Io.

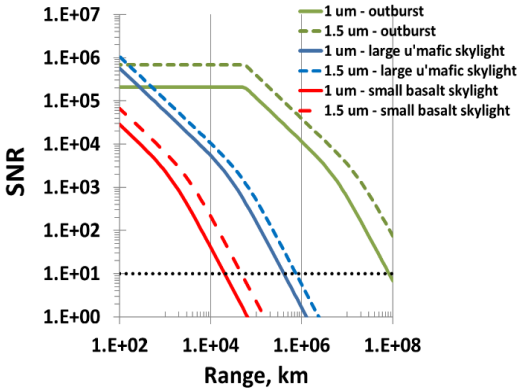

Figure 1. Signal to Noise Ratio (SNR) at 1 and 1.5 μm as a function of range for a large thermal outburst and small lava tube skylights. These eruptions are detectable at SNR values (>10) over a wide range of distances to target. From [2].

1.1 HOT-BIRD and D-ROIC

The "HOT" in HOT-BIRD refers to High Operating Temperature, and "BIRD" refers to Barrier Infrared Detector [8]. This infrared detector technology was recently developed at JPL [8]. We use a novel D-ROIC developed by MIT Lincoln Laboratory with the HOT-BIRD detector. An analogue-to-digital converter and digital counter is placed in each pixel [9]. These digital-pixel readout integrated circuits (D-ROICs) store digital count values related to the photocurrent integrated by the detector. The digital counters do not saturate if their maximum count number is exceeded. Instead, they "roll over" and begin counting again from zero. In this manner, no information is lost; the count number are recovered using real-time processing to correct for rollovers [10]. The combination of HOT-BIRD with the D-ROIC results in an imaging system technology that can cope with the extreme variability,

unpredictability and unknown magnitude of Io's volcanic thermal emission without saturation.

2. Instrument model

Our Excel-based instrument model [2] demonstrates that a short-wavelength infrared instrument on an Io flyby mission can achieve simultaneity of observations by splitting the incoming signal for all relevant eruption processes and still obtain data fast enough to remove uncertain-ties in accurate determination of the highest lava surface temperatures exposed. Examples of SNR values for extreme (both big and small) thermal sources are shown in Figure 1.

3. Deriving eruption temperature

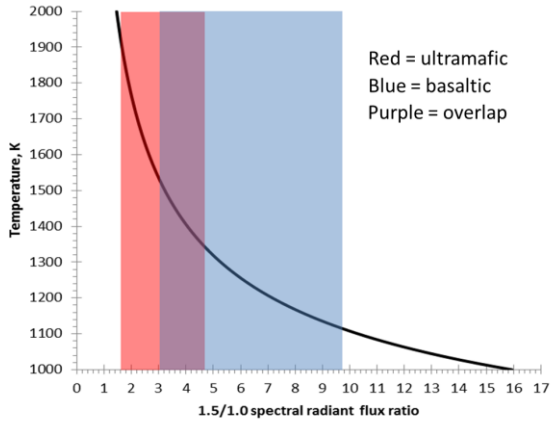

Figure 2. Skylight 1.5-µm:1.0-µm radiant flux ratio as a function of temperature [see 6]. The red area is exclusively ultramafic. Adapted from [2].

We find that observations at 1 and 1.5 µm are sufficient for determining eruption temperature. Even with a ten-way beam split, instrument throughput generates acceptable signal to noise values (Fig. 1) even for the smallest targets. Fig. 2 shows the expected range of the 1.5:1.0 ratio expected for small skylights exposing basalt (blue) and ultramafic lavas (red), with the overlap shown in purple. The ratios are derived from an active skylight thermal emission model [6]. Lava eruption temperature determinations are, of course, also possible with a visible wavelength detector so long as data at different wavelengths are obtained simultaneously and integration time is very short, so as to "freeze" the lava cooling or heating process. This is especially important for examining the thermal emission from lava tube skylights due to rapidly changing viewing geometry during close flybys [6].

Acknowledgements

This work was performed at the Jet Propulsion Laboratory – California Institute of Technology, under contract to NASA. SG thanks the JPL Fellows Fund for support. We thank the NASA PICASSO and Outer Planetary Research Programs for support.
© 2018 Caltech.

References

[1] Keszthelyi, L., et al., 2007. New estimates for Io eruption temperatures: implications for the interior. Icarus 192, 491–502.

[2] Davies, A.G., et al. (2017) A novel technology for measuring the eruption temperature of lavas with remote sensing: application to Io and other planets, JVGR, 343, 1-16.

[3] Veeder, G.J., et al. (2012). Io: volcanic thermal sources and global heat flow. Icarus 219, 701–722.

[4] Veeder, G.J., et al. (2015) Io: heat flow from small volcanic features. Icarus 245, 379–410.

[5] Peale, S.J., et al. (1979) Melting of Io by tidal dissipation. Science 203, 892–894.

[6] Davies, A.G., et al. (2016) Determination of eruption temperature of Io's lavas using lava tube skylights. Icarus 278, 266–278.

[7] Davies, A.G. et al. (2018) Discovery of a Powerful, Transient, Explosive Thermal Event at Marduk Fluctus, Io, in *Galileo* NIMS Data, GRL, 45, 2926-2933.

[8] Ting, D. et al. (2011) Advances in Infrared Photodetectors, Elsevier Acad. Press, 1-57.

[9] Kelly, M., et al. (2005) Design and testing of an all-digital readout integrated circuit for infrared focal plane arrays. Proc. SPIE 5902, p. 105.

[10] Kelly, M., et al. (2015) U.S. Patent 9,270,895.

EPSC Abstracts
Vol. 12, EPSC2018-197, 2018
European Planetary Science Congress 2018
© Author(s) 2018

Growth and Structural Style of Thrust Systems on Mars

Christian Klimczak (1), Corbin L. Kling (2) and Paul K. Byrne (2)
(1) Structural Geology and Geomechanics Group, Department of Geology, University of Georgia, Athens, GA 30602, USA (klimczak@uga.edu), (2) Planetary Research Group, Department of Marine, Earth, and Atmospheric Sciences, North Carolina State University, Raleigh, NC 27612, USA

1. Introduction

Evidence suggests that large thrust fault systems, with lengths greater than the thickness of the brittle lithosphere, are widespread within the southern highlands on Mars [e.g., 1, 2]. As is typical for any large-scale fault, these thrust systems likely consist of complex zones of deformation involving one or more fault planes, a zone of intensely sheared rock (the fault core [3]), and a fault damage zone surrounding the fault core. On Mars, understanding of fault zone complexity and fault rock properties from field observations is limited, such that large faults are generally approximated as a single, large slip plane. However, more detailed knowledge of the growth and structural style of thrust systems on Mars is critical in light of the upcoming NASA InSight mission for understanding the strength properties and seismic behavior of faults in the Martian lithosphere [4].

Sub-surface thrust fault architecture, geometry, and amount of tectonic uplift resulting from cumulative slip on the faults are together expressed at the surface as an asymmetric ridge. This morphology is interpreted as fault-related anticlinal flexures in the hanging wall of the fault, with one steep and one gentle slope, representing the fore– and backlimb, respectively, and a fault surface break at or near the base of that forelimb (Figure 1a). Several such landforms possess a few thousand meters of relief and are hundreds of kilometers long [e.g., 2]. Characterizing the map patterns and along-strike morphology of such landforms provides more information on the three-dimensional shape of their fault planes and slip distributions (described below), which offer clues to fault growth and structural styles of the thrust systems.

2. Growth of Martian Thrust Faults

We studied map patterns and growth geometries of 20 large thrust fault-related landforms across Mars, with a total of 25 individual fault segments, by assessing the changes of topography across the length of each of the mapped landforms [5] (Figure 1b). This methodology is commonly applied to Terran faults, including thrust systems [e.g., 6]. Because of low erosion rates on Mars [7], the observed fault-related topography essentially reflects the cumulative amount of accommodated offset on the faults. The observed topographic variations along the landforms [5] (Figure 1a) may thus be interpreted as cumulative slip distributions. Our results indicate that, although there is great variability in how these faults have grown, their slip distributions can be characterized as either symmetric or asymmetric. Some 14 fault systems show symmetric profiles (Figure 1b, left panel), with six showing asymmetric profiles (Figure 1b, right panel). Supported by our map observations, we interpret many of the asymmetric slip distributions as representing fault growth influenced by interactions with other nearby structures. A few examples may also show fault tip restrictions arising from, for example, changes in material strength from lithology or fracture density [8–9]. Symmetric slip distributions, in contrast, are indicative of fault growth that has largely been unaffected by such barriers or other nearby faults [e.g., 10].

3. Thrust System Structural Style

Large thrust systems are widespread across Mars, and feature a broad range of orientations. They are typically found as isolated landforms that do not show any arrangements in, for instance, long continuous mountain belts with multiple aligned and parallel landforms as major thrust systems on Earth do. The isolated structures show lengths of ~150 to ~400 km with uplifts of 1000 to 2500 m, but the Phlegra Montes, a set of landforms in the northern lowlands, is almost 1400 km long and boast uplifts of as much as 3400 m. All topographic expressions were found to be asymmetric ridges in cross section, with a surface break at the forelimb (e.g., Figure 1a). The lengths and amounts of uplift found for these landforms show that substantial mountain building took place on Mars and, given the widespread

geographic distribution of these landforms across the planet, that it occurred on a global scale.

Mountain building on Earth is either directly or indirectly related to plate tectonics. Whether some primitive form of plate tectonics occurred on Mars is debated [11], but there is no evidence for globally distributed, Earth-style plate tectonics preserved in its geologic record [12]. Mountain building on Mars, if related to some form of plate tectonics, would likely involve structural styles of faulting comparable to thrust belts on Earth, including multiple, long, sinuous thrust fault traces and complex landform morphology. Although the formation of thrust belts, such as found on Mercury [13], does not require plate tectonics, the lack of such morphological evidence supports the view that Earth-style plate tectonics, and associated formation of thrust-belt-style faulting, did not prevail in the geologic history of Mars.

Given that large-scale thrust faults on Mars are thought to penetrate to depths of ≥30 km [2,14,15], and based on the relatively simple map patterns and asymmetric cross-sectional topography of landforms in our study areas, the structural style of the thrust faulting analyzed here is comparable to Terran intra-plate, basement-block faulting and associated fault-propagation folding. Martian thrust systems are thus analogous to faulting associated with the Laramide orogeny in the western United States or the late-Cretaceous block and inversion tectonics in central Europe.

4. Summary and Conclusions

We observe a wide diversity in thrust fault displacement distributions that can be broadly categorized into symmetric and asymmetric shapes. This diversity is likely caused by a combination of factors including regional variations in rock properties and lithospheric structure, as well as fault interaction and linkage. The widespread distribution of these structures across Mars, their broad set of orientations, their straightforward, linear map patterns with only one or a few segments as part of a single major structure, their isolated occurrence, and their simple asymmetric cross-sectional topography do not correspond to Earth-like plate-tectonic-style thrust belts. Instead, our observations support a style of faulting analogous to that of intra-plate basement-block faulting and associated fault-propagation folding of near-surface units. This view will help provide constraints when interpreting fault-induced seismicity detected by the InSight mission, which will land on the Red Planet in November 2018.

5. References

[1] Watters, T. R.: JGR, Vol. 98, pp. 17049–17060, 1993. [2] Egea-González, I. et al.: Icarus, Vol. 288, pp. 53–68, 2017. [3] Caine, J. S. et al.: Geology, Vol. 24, pp. 1025–1028, 1996. [4] Klimczak, C. et al.: LPS XLIX, March 19–23, Abstract #1083, The Woodlands, TX, USA, 2018. [5] Kling, C. L. and Klimczak, C.: LPS XLVII, March 21–25, Abstract #2888, The Woodlands, TX, USA, 2016. [6] Haiyun, B. et al.: JGR, Vol. 123, pp. 2484–2501, 2018. [7] Golombek, M.P. and Bridges, N. T.: JGR, Vol. 105, pp. 1841–1853, 2000. [8] Manighetti, I. et al.: JGR, Vol. 106, pp. 13667–13696, 2001. [9] Davis, K. et al.: JSG, Vol. 27, pp. 1528–1546, 2005. [10] Nicol, A. et al.: JSG, Vol. 18, pp. 235–248, 1996. [11] Barlow, N.: Mars: An Introduction to its Interior, Surface and Atmosphere, Cambridge University Press, 2008. [12] Zuber, M. T.: Nature, Vol. 412, pp. 220–227, 2001. [13] Byrne, P. K. et al.: Nature Geosci., Vol. 7, pp.301–307, 2014. [14] Schultz, R. A., and Watters, T. R.: GRL, Vol. 28, pp. 4659–4662, 2001. [15] Mueller, K. et al.: EPSL, Vol. 408, pp. 100–109, 2014.

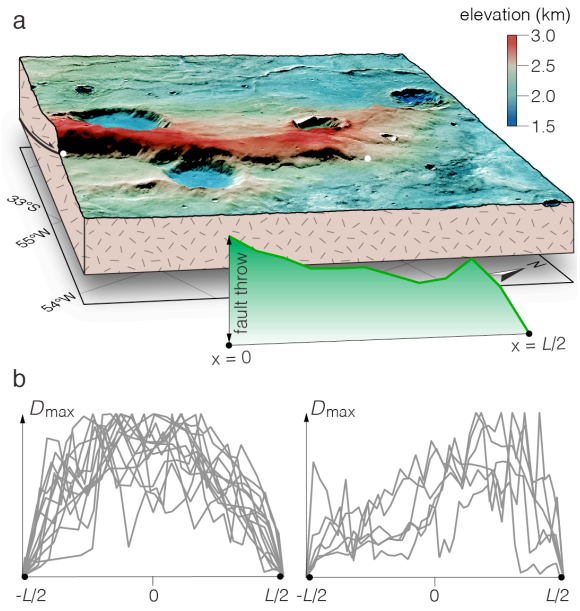

Figure 1. Thrust fault growth on Mars. (a) Block diagram showing the northern half of Ogygis Rupes, an example of a large thrust fault-related landform on Mars. Its slip distribution is shown in the foreground. (b) Symmetric (left) and asymmetric (right) slip distributions normalized by fault length (L) and maximum displacement (D_{max}) of all analyzed structures.

EPSC Abstracts
Vol. 12, EPSC2018-243, 2018
European Planetary Science Congress 2018
© Author(s) 2018

Preliminary petrographic characterization, $^{40}Ar/^{39}Ar$ and CRE ages of Apollo 15 regolith basaltic fragments

Vera Assis Fernandes (1,2), Peter Czaja (1) Lydia Fawcett (2)
(1) Museum für Naturkunde, Leibniz-Institut für Evolutions- und Biodiversitätsforschung, Berlin, Germany, (2) School of Earth and Environmental Sciences, University of Manchester, Manchester, U.K. (veraafernandes@yahoo.com).

Abstract

We present here preliminary results of an integrated study of nine Apollo 15 basaltic fragments found along impact ejecta of small craters in the vicinity of the landing site. The 2-4mm fragments present a wide range of compositions similar to those already defined for Apollo 15, including evidence of an assembly of at least two different lithologies that crystallized at different times. ^{40}Ar-^{39}Ar ages obtained for these 9 fragments range from 3163±9 to 3891±21 Ma Ma, tapping into older ages for samples from the Mare Imbrium.

1. Introduction

Together with the previously reported data on "new" Apollo 17 basaltic regolith fragments, here is reported preliminary work on "new" Apollo 15 basaltic regolith fragments. Like Serenitatis Basin, remote sensing data obtained from lava filled surface within Imbrium Basin presents 30 lava flows distinguished based on their spectrally different compositions [1]. The range in ages based on crater counting statistics is between 2.01 and 3.57 Ga (≥1.6 Ga activity). However, there is currently no information on the chemical diversity of lava flows below the observable ones. Thus, a complete understanding of chemical and isotopic mantle evolution beneath this basin cannot be constrained, yet. Apollo 15 basalt lithologies are divided into olivine, pigeonite, quartz and KREEP types, and green, yellow and orange glasses. The current Apollo 15 volcanic samples age range is narrow comprising about ~200 Ma between 3.16 and 3.40 Ga [2, 3], a ~7 times shorter active period than that suggested by cratering statistics. Acquiring mineralogical and chemical composition and chronological data from different lava types is needed to improve the understanding Mare Imbrium volcanic activity. Here are presented textural, mineral chemical composition and ^{40}Ar-^{39}Ar ages of 9 Apollo 15 2-4 mm regolith fragments collected from impact ejecta of small craters in the vicinity of Stations 6 and 9 & 9A, and from the rim of Spur crater at Station (Table 1). Ejecta from these small craters come from depths greater than any of the Apollo 15 drill-cores. Hence, these fragments potentially sampled material from excavated underlying lava flows and intercalated regolith that potentially included local and regional material (from other flows within Mare Imbrium).

2. Methods

A JEOL JXA 8500A with field emission EMP was used to obtain BSE images and major mineral major element compositions (11 mm working distance, 15 keV power and 15 nA current). A Thermo Scientific Argus VI mass spectrometer was used for ^{40}Ar-^{39}Ar age determination via the IR-laser step-heating technique. The present CRE-ages were calculated using the nominal ^{38}Ar production rate.

3. Samples

Table 1 shows a summary of the preliminary petrographic and chemical characterization of the Apollo 15 regolith basaltic fragments.
⇒**15243,108:** is a vitrophyre containing one large zoned pyroxene ($En_{24-60}Wo_{9-32}Fs_{28-44}$), olivine ($Fo_{60-68}$) and ubiquitous spinel and chromite.
⇒**15385,29** (Fig. 1b): is a coarse olivine basalt containing large olivine crystals (Fo_{57-63}) and large zoned pyroxene ($En_{12-57}Wo_{9-41}Fs_{15-32}$), interstitial plagioclase (An_{90-95}), minor ilmenite, FeS and K-glass.
⇒**15388,29:** resembles the last crystallization stages of a quartz basalt and is composed only of pyroxene ($En_{12-57}Wo_{9-41}Fs_{21-61}$), plagioclase ($An_{89-94}$) and minor spinel.
⇒**15433,94:** has at least two lithologies: 1) a coarser lithology composed of orthopyroxene rimmed by pigeonite ($En_{4-81}Wo_{3-32}Fs_{17-54}$), 2) a finer lithology composed of plagioclase laths (An_{71-89}) and a KREEPy component containing K-spar, K-glasss,

Table 1 Summary of Apollo 15 basaltic regolith samples showing basalt type, texture, mineralogy and major mineral chemical composition.

Sample	Station	Basalt type	Sub-sample	Olivine Fo	Pyroxene En	Pyroxene Wo	Pyroxene Fs	Plagioclase An	Oxide	Other phases	Groundmass
15243,108	6	Olv-vitrophyre	10B	60-68	24-60	9-32	28-44	-	spn, chr	-	✓
15385,29	7	Olivine	11B	57-63	44-63	9-40	15-32	90-95	ilm	tr, K-glass	-
15388,29	7	Pigeonite	7B	-	12-57	9-41	21-61	89-94	spn	-	-
15433,94*	7	Coarse Opx&Plag + KREEP	17B	-	4-81	3-32	17-54	71-89	ilm, spn	bad, trq, K-spar, K-glass, apatite, SiO_2	-
15433,98	7	?	2B	72	47-80	2-39	13-27	82-95	ilm, spn	bad, zir, apt, tr,	-
15533,12	9	Olivine	14B	12-47	22-58	10-34	23-60	87-92	ilm, spn	K-glass, trq	-
15533,14	9	Pigeonite	4B	-	17-68	6-37	25-53	-	chr	-	✓
15534,29	9	Olivine	21B	48-54	43-59	9-34	23-40	89-93	chr, spn	-	-
15639,6	9A	Coarse Olv	6B	32-53	30-59	9-35	21-54	89-91	chr, spn	trq, apt, K-glass, SiO_2	-

apt=apatite; bad=baddeleyite; chr=chromite, ilm=ilmenite; SiO2=silica polymorph; spn=spinel; tr=troilite; trq=tranquiityite; zir=zircon

tranquilityite, baddeleyite, apatite and SiO_2. ⇒**15433,98:** partly resembles olivine fractionate basalt 15676, contains relatively coarser plagioclase (An_{82-95}) and pyroxene ($En_{47-80}Wo_{2-39}Fs_{13-27}$), one having lamellae. The groundmass is composed of equant pyroxene and few olivines surrounded by interstitial plagioclase. Minor phases observed were baddeleyite, zircon, apatite and troilite. ⇒**15533,12:** is a coarse texture basalt resembling the olivine cumulates 15641 and 15663. Zoned pyroxene ($En_{22-58}Wo_{10-34}Fs_{23-60}$), few scattered olivines (Fo_{12-47}), and interstitial plagioclase (An_{87-92}). Minor phases include K-glass and tranquilityite. ⇒**15533,14:** is a vitrophyre composed of quenched groundmass, zoned euhedral pyroxene ($En_{17-68}Wo_{6-37}Fs_{25-53}$), and minor subhedral chromite. ⇒**15534,29:** is a coarse texture basalt resembling olivine cumulates 15641 and 15663. Zoned pyroxene ($En_{43-59}Wo_{9-34}Fs_{23-40}$), scattered olivines ($Fo_{48-54}$), and interstitial plagioclase (An_{89-93}). Minor phases observed are chromite and spinel. ⇒**15639,6:** a coarse texture basalt resembling olivine cumulate 15663. Zoned pyroxene ($En_{30-59}Wo_{9-35}Fs_{21-54}$), scattered olivines ($Fo_{32-53}$), interstitial plagioclase (An_{89-91}), and minor phases are chromite, spinel, tranquilityite, apatite, K-glass and SiO_2.

4. ^{40}Ar-^{39}Ar and CRE age

All data corrected for blank, discrimination, decay of short-lived nucleogenic nuclides (^{37}Ar &^{39}Ar), and where necessary cosmogenic and/or trapped Ar corrections were applied. Ages were obtained from Ar-release spectra, inverse or normal isochrones. ^{40}Ar-^{39}Ar ages (Table 2) range from 3891±21 Ma and 3163±45 Ma, extending the previous age range for Apollo 15 samples by ~200 Ma. and agrees with recently reported older ages from volcanic glasses by [4]. CRE-ages define a range between 101 and 770 Ma suggesting different gardening histories for Apollo 15 regolith samples.

Table 2: Summary table for the ^{40}Ar-^{39}Ar age determinaiton measurements including Cosmic-ray Exposure Age. Ages reported at 2σ.

Sample	Weight (mg)	Age Spectra (Ma)	Age Spectra %^{39}Ar	Age Spectra low-T reset	3-isotope plots Norm. Iso (Ma)	3-isotope plots Inv. Iso (Ma)	Nominal CRE-age
15243,108	3.27	3407±15	74	-	3409±23	3390±18	611
15385,29	4.44	3414±26	83	-	3423±33	3428±49	433
15388,29	4.48	3288±500	46	-	-	3353±76	770
15433,94*	4.37	-	-	-	2049±10 3136±10 - 3596±32	low-T interm-T high-T last 6	140
15433,98	4.21	3854±20	32	≤3731	-	3891±21	583
15533,12	4.17	3410±420	68	-	-	3289±48	212
15533,14	4.10	3308±22	85	-	3307±33	-	101
15534,29	3.79	3260±25	88	-	3232±42	3258±23	197
15639,6	3.25	3168±35	62	-	3163±45	3163±9	299

***This sample is composed of at least 2 distinct lithologies: 1) an older coarse texture of opx and plag, and 2) a younger finer texture of KREEPy material, resulting in a multi-Ar domain release.**

Acknowledgements: Project funded by DFG FE1523/3-1. Sam Bell thanked for sharing her Apollo 15 samples BSE images.

References: [1] Hiesinger et al. (2011) Geol. Soc. of America Sp. Pap. 477, 1-51. [2] Nyquist & Shih (1992) GCA 56, 2213-2234. [3] Snyder et al. (2000) *In* Origin of the Earth and Moon, 361-396. [4] Zellner et al. (2018) 49th LPSC, abst.# 2356.

EPSC Abstracts
Vol. 12, EPSC2018-377, 2018
European Planetary Science Congress 2018
© Author(s) 2018

Geological Characteristics of Von Kármán Crater, Northwestern South Pole-Aitken Basin: Chang'E-4 Landing Site Region

Jun Huang (1), Zhiyong Xiao (1), Jessica Flahaut (2,3), Mélissa Martinot (4,5), James Head (6), Xiao Xiao (1), Minggang Xie (7), Long Xiao (1)
(1) State Key Laboratory of Geological Processes and Mineral Resources, Planetary Science Institute, School of Earth Sciences, China University of Geosciences, Wuhan 430074, China, (2) CRPG-CNRS/Université de Lorraine, 54500 Vandœuvre-lès-Nancy, France, (3) IRAP-CNRS-CNES/Université Paul Sabatier, 31400 Toulouse, France, (4) Faculty of Science, Vrije Universiteit Amsterdam, Amsterdam, The Netherlands, (5) Université Lyon 1, ENS-Lyon, CNRS, UMR 5276 LGL-TPE, Villeurbanne, France, (6) Department of Earth, Environmental and Planetary Sciences, Brown University, Providence, RI, 02912 USA, (7) Space Science Institute, Macau University of Science and Technology, Macau, China (junhuang@cug.edu.cn)

Abstract

Von Kármán crater (diameter =~186 km), lying in the northwestern South Pole-Aitken basin, was formed in the pre-Nectarian. The Von Kármán crater floor was subsequently flooded with one or several generations of mare basalts during the Imbrian period. Numerous subsequent impact craters in the surrounding region delivered ejecta to the floor, together forming a rich sample of the SPA basin and farside geologic history. We studied in detail the targeted landing region (45.0–46.0 °S, 176.4–178.8 °E) of the 2018 Chinese lunar mission Chang'E-4, within the Von Kármán crater. The topography of the landing region is generally flat at a baseline of ~60 m. Secondary craters and ejecta materials have covered most of the mare unit, and can be traced back to at least four source craters (Finsen, Von Kármán L, Von Kármán L' and Antoniadi) based on preferential spatial orientations and crosscutting relationships. Extensive sinuous ridges and troughs are identified spatially related to Ba Jie crater (diameter = ~4 km). Reflectance spectral variations due to difference in both composition and physical properties are observed among the ejecta from various-sized craters on the mare unit. The composition trends were used together with crater scaling relationships and estimates of regolith thickness to reconstruct the subsurface stratigraphy. The results reveal a complex geological history of the landing region, and set the framework for the in-situ measurements of the CE-4 mission, which will provide unique insights into the compositions of farside mare basalt, SPA compositional zone, including SPA compositional anomaly and Mg-pyroxene annulus, regolith evolution and the lunar space environment.

1. Introduction

In 2018, the Chinese lunar mission Chang'E-4 (CE-4) (Wu et al., 2017) will explore the SPA basin. It will be the first in-situ exploration of the farside of the Moon. The selected landing region for CE-4 (45 °S - 46 °S, 176.4 °E - 178.8 °E) (Wu et al., 2017) is located on the southern floor of the Von Kármán crater. In-situ exploration within the Von Kármán landing region will bring unprecedented imaging, spectral, radar and low-frequency radio spectral data for the landing region, and it will greatly improve our understanding about the compositions of farside mare basalt, SPA compositional zones including SPA compositional anomaly and Mg-pyroxene annulus, regolith evolution and the lunar space environment. Indeed, the U.S. National Research Council (2007) has identified key scientific priorities for future lunar exploration that can be addressed from the Von Kármán crater, including the possibility to study the existence and extent of differentiation of the SPA melt sheet (Morrison et al., 1998; Nakamura et al., 2009; Vaughan and Head, 2014) and possible exposed upper mantle materials (Melosh et al., 2017; Moriarty and Pieters, 2018). In this study, we have 1) investigated the geological characteristics of the landing region using available remote sensing data including topography, high-resolution imaging, and reflectance spectral data, 2) identified targets of high scientific interests, and 3) proposed testable hypothesis for the CE-4 mission.

2. Methods

We analyzed the local geology using the Lunar Reconnaissance Orbiter Camera (LROC) Wide Angle Camera (WAC) mosaic (100 m/pix) for regional context (Robinson et al., 2010), Kaguya Multiband Imager (MI) 750 nm reflectance mosaic (14 m/pix) for albedo variations (Ohtake et al., 2008), Terrain Camera (TC) morning mosaic (7 m/pix) for local context (Kato et al., 2010), and LROC Narrow Angle Camera (NAC) images (0.5-1.6 m/pix) for small geological feature identification. Topographic analyses were performed using the merged Digital Elevation Model (DEM) that is derived from the LRO Lunar Orbiter Laser Altimeter (LOLA) (Smith et al., 2010) and Kaguya TC data (SLDEM: 59 m/pix) (Barker et al., 2016). We produced a slope map for the landing region using SLDEM at a 59 m scale.

3. Figures

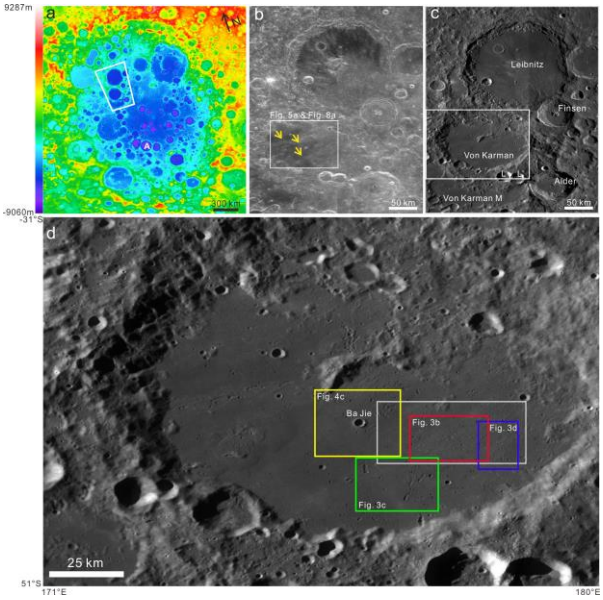

Figure 1: Landing Region of Chang'E-4 Mission

4. Summary and Conclusions

The Chinese CE-4 lunar mission will be the first in-situ exploration to explore the surface of the Moon and study its environment on the farside. The selected landing area is located in the southern portion of the Von Kármán crater, on the top of the infilling mare unit, and within the SPA basin (Fig. 1). We characterized the terrain and geological characteristics of the landing region using multi-source remote sensing datasets. The main conclusions are as follows: The landing region is generally flat at a length scale of 59 m and located within a rather homogenous mare unit; The absolute model age of the mare unit within Von Kármán crater is 3.6 Ga (+.09, -.2); Secondary craters have almost covered the entire landing area.; The thickness of the regolith is estimated to be ~2.5 m to 7.5 m in the landing area; Extensive sinuous ridges and sinuous troughs are identified in the landing area. They are related to Ba Jie crater spatially. Spectral variations among the ejecta of craters of various sizes reveal the subsurface structures.

Acknowledgements

LRO NAC and WAC data, Chandrayaan-1 M3 data were downloaded from the PDS (https://pds.nasa.gov/). MI and TC data were downloaded from the SELENE archive (http://darts.isas.jaxa.jp/planet/pdap/selene/). The data of regolith estimation and subsurface reconstruction are available in the supplementary materials. Crater count data can be acquired on request to Z.X. J. H. was supported by National Scientific Foundation of China (No. 41773061), the Fundamental Research Funds for the Central Universities, China University of Geosciences (Wuhan) (No. CUGL160402 and No. CUG2017G02). Z.X. was supported by National Scientific Foundation of China (No. 41773063). The work of J. F. is supported by the CNES (Luna/ExoMars APR). The work of M. M. was supported by a Netherlands Organization for Scientific Research (NWO) grant. The authors also thank Dr. Qiong Wang for the discussion of the landing region.

References

Please see the reference list in Jun Huang et al., 2018, Geological Characteristics of Von Kármán Crater, Northwestern South Pole-Aitken Basin: Chang'E-4 Landing Site Region, JGR-Planets, In press.

EPSC Abstracts
Vol. 12, EPSC2018-384, 2018
European Planetary Science Congress 2018
© Author(s) 2018

The Idunn Mons-Olapa Chasma system as the candidate site for studying ongoing volcanotectonic activity on Venus

Piero D'Incecco (1), Ivan López (2), Attila Komjathy (3), James A. Cutts (3), Siddharth Krishnamoorthy (3). (1) Arctic Planetary Science Institute, Berlin, Germany (piero.dincecco@planetaryscience.de), (2) Universidad Rey Juan Carlos, Madrid, Spain, (3) Jet Propulsion Laboratory, California Institute of Technology, Pasadena, California (US)

1. Introduction

Previous works have identified Idunn Mons – the 200 km diameter large volcano located at Imdr Regio – as the possible site of recent volcanism on Venus [1,2].
Here, we investigate with greater detail the geology of this area, with a particular focus on the tectonic interaction between Idunn Mons and Olapa Chasma, the rift zone where the volcano is located. In fact, the first indications from our mapping suggest that – being a site of recently active volcanism – Idunn Mons would consequently be a site of active tectonism as well.
The close relation between an eventual ongoing volcanic activity and active tectonism makes Idunn Mons as a credible candidate site for future missions, whose goal is that of studying volcanism and surface geochemistry [3,4] as well as the seismic activity [5] on Venus.

2. Methodologies

The preliminary assessment was conducted relying on the 1 μm emissivity anomalies observed by the VIRTIS instrument of the Venus Express mission and analysed in detail by previous studies [1,2].
For the geologic interpretation, we base on the Magellan right and left looking radar images at the highest available resolution (75 m/px). The mapping is performed through a combination of GIS and vector graphics editor software.

3. Geologic context

3.1 Morphology

Based on the existing morphologic classification of the large volcanoes on Venus, Idunn Mons belong to the class VII, which includes the volcanic edifices arranged along the axis of a rift trend [6].
Idunn Mons presents a flat-topped summit that can be observed in backscatter differences in the left-looking image and more clearly in the right-looking image (Fig. 1). On Earth, the formation of volcanoes with flat-topped morphology is still object of debate and includes two main hypotheses: constructional [i.e., 7] and destructive/erosional [8].
In the constructional hypothesis scenario, the morphology of the volcano is the result of lava flow eruptions originating from a ring dyke on the top of the edifice [7]. However, Idunn Mons lacks evidence of having circular fractures on its summit that would be the evidence for the presence of ring dykes under the surface (Fig. 1).
In the destructive (or erosional) hypothesis, the flat-topped morphology of the volcano would be the result of alternating effusive and erosional episodes, where the erosion produced the formation of a stepped topography over which late volcanic effusive materials are emplaced, adapting to and mimicking the flat and stepped topography that resulted from the previous erosional stage [8, 9].

3.2 Tectonism

While it is clear that the wrinkle ridges in the surroundings of the study area predate the formation of both Olapa Chasma and Idunn Mons, the tectonic setting of the volcano is closely interconnected with that of the rift zone.
In fact, the fractures characterizing Idunn Mons are characterized by an "hour-glass" pattern that is typical of areas where the stress fields forming a rift interact with the stress fields related to the eruptive episodes originating the volcanic edifice within the rift.
The syntectonic character of the Idunn Mons and Olapa Chasma is shown by the fact that some lava flows in the vicinity of the top and eastern flank of the volcano predate while other lava flows get locally disrupted by the rift-related fractures, disposed radially and concentrically to its summit (Fig. 2).
In this scenario, also the collapse events that we observe on the summit and flanks of the volcanic edifice would be just due to the volcano-rift tectonic interaction. This would also explain the flat-topped morphology of Idunn Mons.

For this reason, the tectonic processes behind the formation of Idunn Mons and Olapa Chasma are most likely recent and synchronous and we talk about Idunn Mons-Olapa Chasma (IMOC) system.

4. Overview

Previous studies based on the analysis of the Venus Express 1 μm emissivity indicated Idunn Mons as a recently active volcano [1,2].
Our detailed geologic analysis of the study area highlights the syntectonic charater of the IMOC system. Hence, the IMOC system could be volcanically as well as tectonically active.
For this reason, we propose this area as the candidate site for the mission concepts which are currently being proposed, involving both in-situ geochemical analyses performed by landers [3,4] and the detection of Venus-quakes associated with volcanic eruptions [5].

References

[1] Smrekar, S. E., et al., 2010. Recent hot-spot volcanism from VIRTIS Emissivity data. Science, 328, 5978, 605-608, doi: 10.1126/science.1186785.

[2] D'Incecco, P., et al., 2016. Idunn Mons on Venus: location and extent of recently active lava flows. Planetary and Space Science journal, available online 21 December 2016, ISSN 0032-0633, https://doi.org/10.1016/j.pss.2016.12.002.

[3] Glaze, L., et al., 2017. VICI: Venus In situ Composition Investigation, #EPSC2017-346, http://adsabs.harvard.edu/abs/2017EPSC...11..346G.

[4] Zasova, L., et al., 2017. Joint IKI/ROSCOSMOS - NASA Science Definition Team and concept mission to Venus based on Venera-D, #EPSC2017-296-1, http://adsabs.harvard.edu/abs/2017EPSC...11..296Z.

[5] Komjathy, A., et al., 2018. Remote sensing of seismic activity on Venus using a small spacecraft: initial modeling results, LPSC #1731, https://www.hou.usra.edu/meetings/lpsc2018/pdf/1731.pdf.

[6] Head, J. W., et al., 1992. Venus volcanism: Classification of volcanic features and structures, associations, and global distribution from Magellan data, Journal of Geophysical Research, v. 97, no. E8, p. 13,153-13,197.

[7] Simkin, T., 1972. Origin of some flat-topped volcanoes and guyots. Geol. Soc. Am. Mem. 132, 183–194.

[8] Rowland, S. K., et al., 1994. Galapagos Islands: Erosion as a possible mechanism for the generation of steep-sided basaltic volcanoes, Bull. Volcanol., 56, 271-283, 1994.

[9] López, I., 2011. Embayed intermediate volcanoes on Venus: Implications for the evolution of the volcanic plains, Icarus, Volume 213, Issue 1, p. 73-85, doi: https://doi.org/10.1016/j.icarus.2011.02.022.

5. Figures

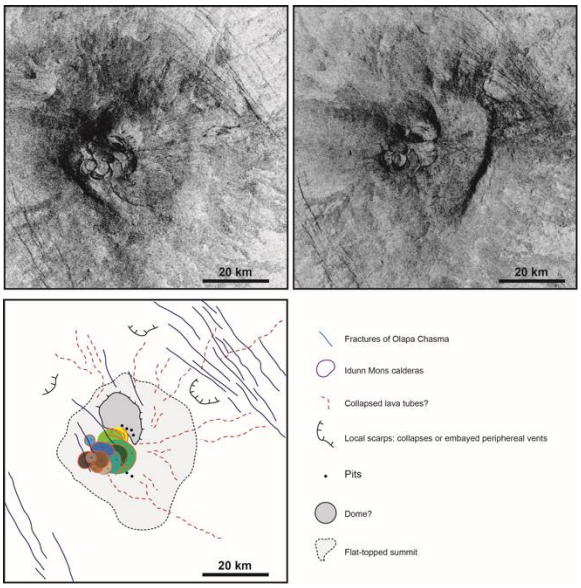

Figure 1 - The summit of Idunn Mons

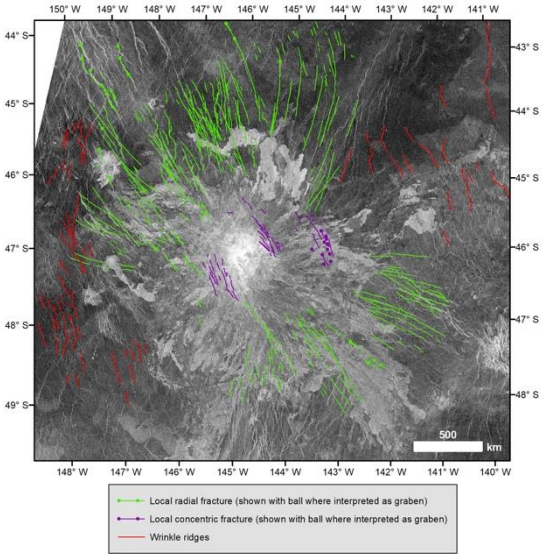

Figure 2 - Tectonic setting of the Idunn Mons-Olapa Chasma (IMOC) system

EPSC Abstracts
Vol. 12, EPSC2018-430, 2018
European Planetary Science Congress 2018
© Author(s) 2018

Deep tectonics exposed in northern Valles Marineris, Mars

Joanna Gurgurewicz and Daniel Mège
Space Research Centre, Polish Academy of Sciences, Warsaw, Poland (jgur@cbk.waw.pl, dmege@cbk.waw.pl)

Abstract

Brittle-plastic, NE-SW oriented dextral shear zones are exposed in the deepest parts of Ophir Chasma and Hebes Chasma. We describe one of the Ophir Chasma shear zones and explore some implications for the geologic evolution of Valles Marineris and Tharsis.

1. Introduction

Oblique strike-slip faulting is ubiquitous in terrestrial rifts, where on continents it appears to be frequently controlled by older fabric, e.g. [1]. Wilkins and Schultz suggested that oblique faults explain the blunt shape of the Valles Marineris troughs, along which kinematics would be extensional rather than strike-slip [2]. HiRISE images reveal the existence of oblique tectonic structures in the northern troughs of Valles Marineris. C-S fabrics are common and point to strike-slip kinematics. Further, they indicate deformation in the brittle-plastic field, consistent with the width of the sheared zones, up to kilometres. These observations make necessary that erosion has been a major trough formation agent in northern Valles Marineris. They also reveal new tectonic elements that need to be considered while reconstructing the evolution of the Tharsis dome.

2. Brittle-plastic shear zones

A survey of HiRISE images available in the deepest parts of Ophir Chasma and Hebes Chasma has revealed several exposures of shear zones (Figure 1) trending NE-SW. Figure 2 shows an example of interpretation in one of these shear zones, located in eastern Ophir Chasma. The area is dominantly covered by recent deposits, including a mantle of dark material, dunes, and landslide deposits from the northern Ophir Chasma wall. The shear zone is exposed in hard, light-toned, unstratified rock. Fractures are also apparent in the dark material, although subdued. The shear zone orientation is emphasized by C shears, and dextral kinematics is demonstrated by S shears associated with the C and also C' shears.

The C-S fabric indicates brittle-plastic deformation, requiring pressure and temperature conditions that could probably not be met at the surface in the history of Mars. Shear zone width is up to several kilometres, and also denotes formation at depth.

The length of the shear zone exposures is up to 10 kilometres. Shear zone displacements are not known; nevertheless, in terrestrial conditions, shear zones of similar width have displacement one order larger than width [3].

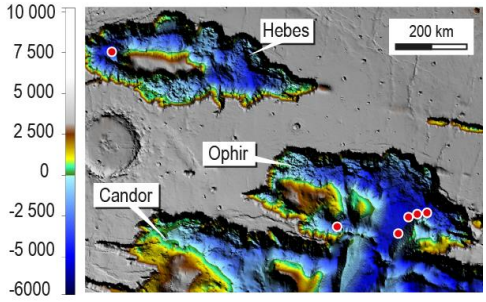

Figure 1: Location of brittle-plastic shear zones identified in Valles Marineris. Exposures are indicated by red dots. The base map is from HRSC digital elevation model.

3. Tectonic significance

Shear zone kinematics is consistent with Valles Marineris crustal stretching perpendicular to the main troughs (Figure 2). The role of tectonic extension in the formation of the northern troughs of Valles Marineris has been questioned though due to the lack of obvious brittle structures exposed at the surface [4]. Of trough formation by collapse [5], vertical subsidence [6], and erosion [7], the latter is consistent with the observations reported here. Deep subglacial erosion inferred from deep dyke exposures in Ophir Chasma [7] as well as glacial landsystem identification in other troughs [8] explain the present shear zone exposures. Giving their thickness and displacement-length scaling of faults [9], the shear zones are regional scale and therefore cannot be neglected in future Tharsis palaeotectonic reconstructions.

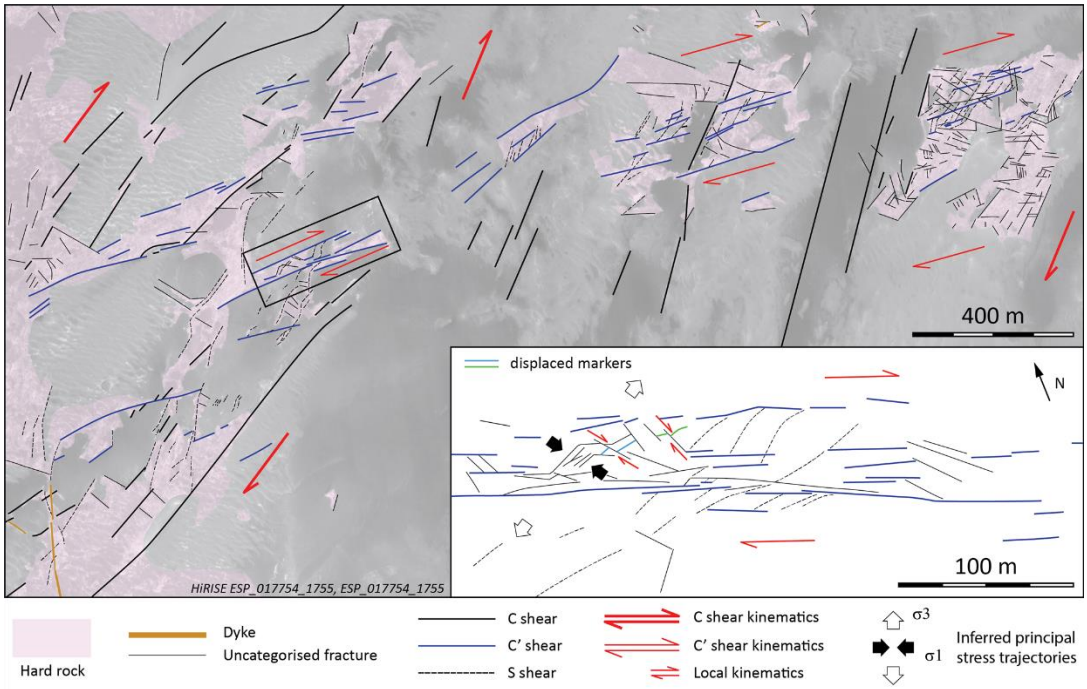

Figure 2: Geometry and kinematics of brittle-plastic shear zone in eastern Ophir Chasma.

4. Conclusions

The shear zone in eastern Ophir Chasma has structural features and size similar to e.g. the Gemini fault zone in the Sierra Nevada, which was developed at a well constrained depth of 8-11 km [10], and similarly is exposed due to glacial erosion. Other brittle-plastic shear zones have been mapped in northern Valles Marineris [11]. None has been identified in the southern troughs, perhaps because sedimentary accumulations are pervasive, or because they are restricted to the northern troughs. In the latter case, the connection between shear zones and trough formation is to be clarified. Kinematics is consistent with Valles Marineris rifting even though evidence of rift border faults is missing in the northern troughs. Mineralogical investigations are underway. Implications for Tharsis evolution are to be explored.

Acknowledgements

This work was funded by the OPUS/V-MACS project no. 2015/17/B/ST10/03426 of the National Science Centre, Poland.

References

[1] Bellahsen, N. et al.: Pre-existing oblique transfer zones and transfer/transform relationships in continental margins: New insights from the southeastern Gulf of Aden, Socotra Island, Yemen, Tectonophysics, Vol. 607, pp. 32-50, 2013. [2] Wilkins, S.J. and Schultz, R.A.: Cross faults in extensional settings: Stress triggering, displacement localization, and implications for the origin of blunt troughs at Valles Marineris, Mars, J. Geophys. Res., Vol. 108(E6), 5056, 2003. [3] Fossen, H.: Structural geology, Cambridge Univ. Press, 2016. [4] Schultz, R.A.: Multiple-process origin of Valles Marineris basins and troughs, Mars, Planet. Space Sci., Vol. 46, pp. 827-834, 1998. [5] Tanaka, K.L. and Golombek, M.P.: Martian tension fractures and the formation of grabens and collapse features at Valles Marineris, Proc. 19th LPSC, pp. 383-396, 1989. [6] Andrews-Hanna, J.C.: The formation of Valles Marineris: 1. Tectonic architecture and the relative roles of extension and subsidence, J. Geophys. Res., Vol. 117, E03006, 2012. [7] Mège, D. et al.: Deep dyke exposures in northern Valles Marineris highlight the significance of erosion in chasma genesis, EPSC Abstracts, Vol. 11, EPSC2017-326, 2017. [8] Gourronc, M. et al.: One million cubic kilometers of fossil ice in Valles Marineris: relicts of a 3.5 Gy old glacial landsystem along the Martian equator, Geomorphology, Vol. 204, pp. 235-255, 2014. [9] Schultz, R.A. et al.: Displacement-length scaling relations for faults on the terrestrial planets, J. Struct. Geol., Vol. 28, pp. 2182-2193, 2006. [10] Pachell, M.A. and Evans, J.P.: Structural analysis of the Gemini strike-slip fault zone, Central Sierra Nevada, California., J. Struct. Geol., Vol. 24, pp. 1903-1924, 2002. [11] Mège, D. and Gurgurewicz, J.: Mapping of regional C-C'-S shear zones on the floor of Valles Marineris troughs, this conference.

EPSC Abstracts
Vol. 12, EPSC2018-577, 2018
European Planetary Science Congress 2018
© Author(s) 2018

Evolution of tectonics of Enceladus

L. Czechowski[1].
[1]University of Warsaw, Faculty of Physics, Institute of Geophysics, ul. Pasteura 5, 02-093 Poland (lczech@op.pl).

Introduction: Enceladus, a satellite of Saturn, is the smallest celestial body in the Solar System where endogenic activity is observed in the form of cryovolcanism. It is concentrated in the South Polar Terrain (SPT) where the mass is ejected into space with the rate ~200 kg/s [e.g. 1, 2, 3]. We follow here our previous suggestions that this mass loss is a main driving mechanism of the Enceladus' tectonics [1, 2].

Present activities: The loss of matter from the body's interior should lead to global compression of the crust. Typical effects of compression are: thrust faults, folding and subduction [5]. However, such forms are not dominant on Enceladus. In previous presentations we proposed special tectonic model that could explain this paradox [1, 2, 5] and Fig. 1.

The volatiles escape from the hot region (through the fractures) forming plumes in the space. The loss of the volatiles results in a void and motion of matter into the hot region to fill the void *in statu nascendi*. The motion includes – Fig. 1:
(i) subsidence of the 'lithosphere' of South Polar Terrain,
(ii) flow of the matter in the mantle,
(iii) motion of plates adjacent to SPT towards the active region.

The motion towards the active region mentioned in (iii) could lead to compression of STP. However, the sinking of the STP plate reduces essentially compressive forces acting from the plates surrounding the STP region. Therefore, the termal processes below tiger stripes are sufficient to keep open the active fractures. Note that the present situation in STP is similar to situation of the Philippine Plate, where back-arc spreading is observed (back arc spreading indicates extensive forces).

Of course, the continuous loss of mass will cause eventually the increase of compression forces, which will ultimately lead to closing fissures and stopping activity in the STP region.

A new activity center will probably be created in the oval region given in Fig. 3. We believe that it is a periodic process. The activity in the present place will be decreasing and a new center of activity will be formed. Note that the ovoid-shaped depression down to 2 km deep, of size 200×140 km with the center at 200E, 15S is a good candidate for this future center. The depression indicates the partial melting of the mantle. It could lead to an increase of tidal heating.

The heating will lead to the emergence of strong convection currents which, acting on the shell, lead to the formation of fissures similar to the current tiger stripes.

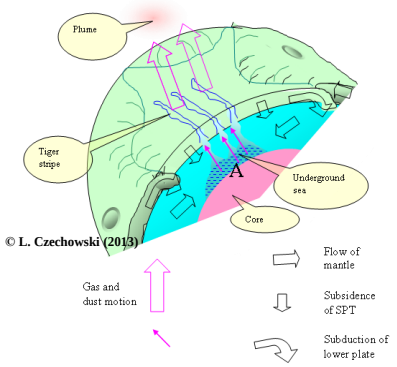

Figure 1: A scheme of suggested processes in the activity center (after [1]). Note that the present situation in STP is similar to situation of the Philippine Plate, where back-arc spreading is observed.

Proto-Enceladus hypotheses: The mass of matter ejected in space by volcanic activity of Enceladus is 200 kg s^{-1}. It means that just after the accretion, Enceladus could be substantially larger. We will refer here this larger body as proto-Enceladus [2]. Two assumptions could be used for calculation of the size of proto-Enceladus: (i) the present rate of mass out flow could be treated as the average or (ii) densities of proto-Enceladus and Mimas were the same because the satellites accreted in the same part of the nebula. Both approaches give similar size of proto-Enceladus [2].

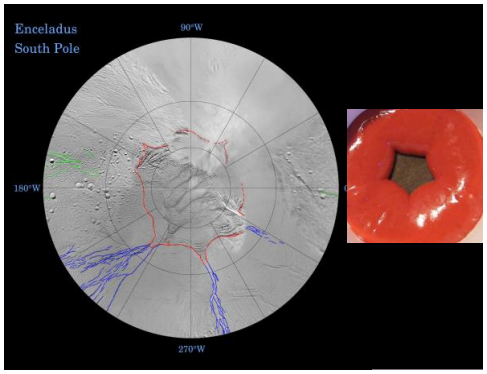

Figure 2. The image of STP (left hand side, after NASA). Laboratory model of subsidence is on the right part of the figure [5]. The subsidency of the central plate reduces significantly compressional forces resulting from interaction with otaczjącyh płyt.

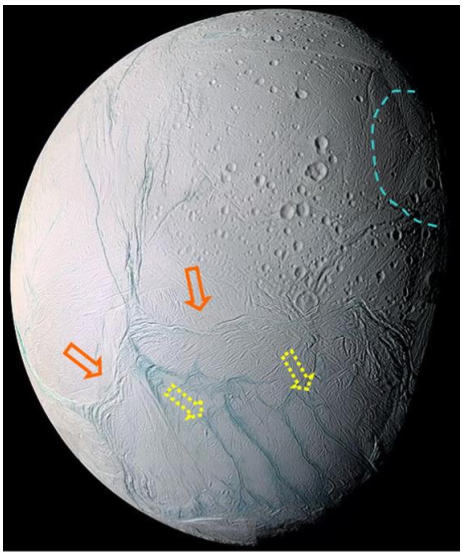
Figure 3. Surface features in the cryovolcanic center (SPT) of Enceladus (NASA, PIA06254). Solid arrows show the arcuate scarps convex southward. Analogy with terrestrial subduction zones suggests that the polar plate is there subducted- e.g. [1]. Dashed arrows indicate two tiger stripes. Blue dashed line shows an ovoid depression which may be an activity center in the future as suggested by [1].

There are some traces of past activity on the surface of Enceladus [4]. The traces could be interpreted as indication that the past activity was similar to the present one (similar features), but we do not know how old are these traces. They could be relatively young.

.**Acknowledgements:** The research is partly supported by BST funds of the University of Warsaw. We are grateful also to the ICM.

References:

[1] Czechowski, L. (2014) Enceladus - the vanishing satellite presenting in EGU 2014, Vienna.
[2] Czechowski, L. (2014) Planet. Sp. Sc. 104, 185-199
[3] Kargel, J.S. (2006) Enceladus: Cosmic gymnast, volatile miniworld. *Science* 311, 1389–1391.
[4] Spencer, J. R., *et al*. (2009), Enceladus: An Active Cryovolcanic Satellite, in: M.K. Dougherty et al. (eds.), *Saturn from Cassini-Huygens*, Springer, Sciencep. 683.
[5] L. Czechowski (2017) Present and future tectonics of Enceladus. Presented in EPSC 2017.

EPSC Abstracts
Vol. 12, EPSC2018-609, 2018
European Planetary Science Congress 2018
© Author(s) 2018

A new look at the Moon using Chang'e-2 microwave radiometer data.

Roberto Bugiolacchi, G-P Hu, and K. L. Chan.
Space Science Laboratory, M.U.S.T., Avenida Wai Long, Taipa, Macau, (**rbugiolacchi@must.edu.mo**)

Abstract

Microwave data obtained from orbit open a new avenue of investigation of the lunar surface properties, potentially down to several meters depth. The first results reveal a distribution of mare materials that hints to late igneous processes affecting both Oceanus Procellarum and Mare Imbrium, within the alleged Procellarum Basin.

1. Introduction

By virtue of its longer wavelength in comparison to UV-VIS-IR, microwave radiation carries information from deeper into the surface and can extend to several times the observation wavelength. Moreover, passive microwave measurements can be carried out during nighttime and in shadowed regions. Most observations of the lunar surface in these frequencies were Earth-based but they helped develop theoretical models to obtain the brightness temperature (TB) of the lunar surface and derive several of physical parameters including heat flow [1]. In this paper we preview the results from a new investigative approach that takes advantage of global lunar microwave data obtained from the Chang'E-2 mission (CE-2). The multi-channel radiometer worked at four different frequencies (about 37, 19, 8, and 3 GHz), probing increasingly deeper into the surface.

The area under investigation encompasses Mare Imbrium and Oceanus Procellarum in the west. Our work focuses on TB differences between a few centimeters regolith thickness (37 GHz) to several meters (3 GHz), taken at (lunar) midnight.

2. Data and method

3. The Level 2C Chang'E-2 (CE-2) Microwave RadioMeter (MRMs) data [2-3] was used in this study, following system calibration and geometric correction with Planetary Data System [4]. The MRM underwent onboard adjustments to ensure its reliability and accuracy using a two-point calibration method (for details see [2-5-6]). We used spherical harmonic fits for the Brightness Temperature (TB) variations with local time [6] to suppress the lunar phase effect. Normalized TBs at midnight were chosen to minimise the topographic effects on the emission [7]. We selected the widest range possible of data from the four frequencies available (3 and 37 GHz) to compare the average thermal emission at different depths within the lunar regolith (centimeters range for 37 GHz, 0.81 cm wavelength, to several meters at 3 GHz, 10 cm wavelength). The penetration depth mainly depends on wavelength but also on the bulk density and loss tangent of the lunar regolith.

Cooler areas both in the 3 and 37 GHz bands are governed by the ilmenite ($FeTiO_3$) content in the regolith, which, due to the shallow penetration, blocks the deeper warmer contribution to the surface. The combination of the rocks and ilmenite appears as relative low-temperature regions (i.e., Aristarchus and north Imbrium's highlands). 'Hot' spots in the 3 GHz map are related to the ilmenite-poor composition and the rock distribution.

In order to investigate further the thermal properties of the subsurface materials the 37 GHz thermal data were subtracted from the 3 GHz to produce a TB difference map (Fig. 1).

4. Results

Mare flows within Mare Imbrium (MI) have been the focus of much research for over 40 years [e.g. 10] and still ongoing. Oceanus Procellarum (OP) does not share the same level of scrutiny but flows were mapped by [9] up to the inferred south-western rim of the Imbrium Basin (Fig. 1). The microwave map shows sharp temperature (differences) gradients that closely follow surficial and reflectance spectra recognized within MI by [10] and confirmed by several studies that followed. However, the TB map suggests that the high-Ti mare flow mapped as 'I'

does not have an equivalent microwave signature. Likewise, we find no 'thermal lows' south of Lambert crater either. Instead, the relatively cooled subsurface can be traced as a single unit down to the Reiner crater. There is general agreement between the OP mare flow distribution marked as 'Sharp' by [9] and this work. Most available titanium maps [e.g. 13], which represent the TiO_2 wt% of the top millimetre of the lunar surface, show a low-Ti region radial to Aristarchus, including a large area separating the continuous 'blue' TB feature be-tween OP with MI. It is likely that ejecta from the young crater might have scattered excavated low-Ti materials over this area. The largest TB differences broadly correspond to the core of flow 'II' [10] and the Marius region in OP. The 'Telemann' (North) unit corresponds to an area that has reached thermal equilibrium between surface and sub-surface regolith.

The ('white') areas with the largest TB differences correspond to craters Aristarchus, Reiner and the south rim of Copernicus. These are covered with debris and impact melts from the relative recent impacts; the southern part of Copernicus differs from the northern section by having a much higher iron content [14], due probably to a larger presence of impact melt with similar composition to basalt.

5. Summary and Conclusions

This work represents just a preliminary look at the high-quality microwave data produced by the MRM instruments. Together with a qualitative analysis of spatial distribution of TB differences, progress is being made to extract quantitative data relating to several physical parameters, including ilmenite content, rocks distribution, and craters age estimation.

Acknowledgements

Research supported by grant number 119/2017/A3.

References

[1] Keihm S. J. and Langseth M. G. (1975) Science, 187, 64-66.
[2] Zheng Y. C. et al. (2012) Icarus, 219, 194-210.
[3] NAO, CAS, accessed Feb 29, 2016. //moon.bao.ac.cn/ceweb/datasrv/dmsce1.jsp.
[4] McMahon S. K. (1996) Planet. & Space Sci., 44, 3-12.
[5] Chan K. L. et al. (2010) Earth and Planet. Sci. Lett., 295, 1-2, 287-291.
[6] Wang Z. Z. et al. (2010) Science China: Earth sci-ences. 53, 1392-1406.
[7] Hu G. et al. (2014) IEEE Transactions on Geosci-ence and Remote Sensing, 52, 8, 4499-4510.
[8] Hu G. et al. (2017) Icarus, 294, 72-80.
[9] Whitford-Stark J. L. and Head J. W. (1980) J. Gephys. Res., 85(B11), 6579-6609.
[10] Schaber G. G. (1973) Proc. LPSC, 4(1), 73-92.
[11] Lee E. M. et al. (2009) LPS XL, Abstract #2445.
[12] U.S. Geol. Surv. (2003) LPSC. Series I-2769.
[13] Sato H. et al. (2017) Icarus, 296, 216-238.
[14] Bugiolacchi R. et al. (2011) Icarus, 213, 43-63.

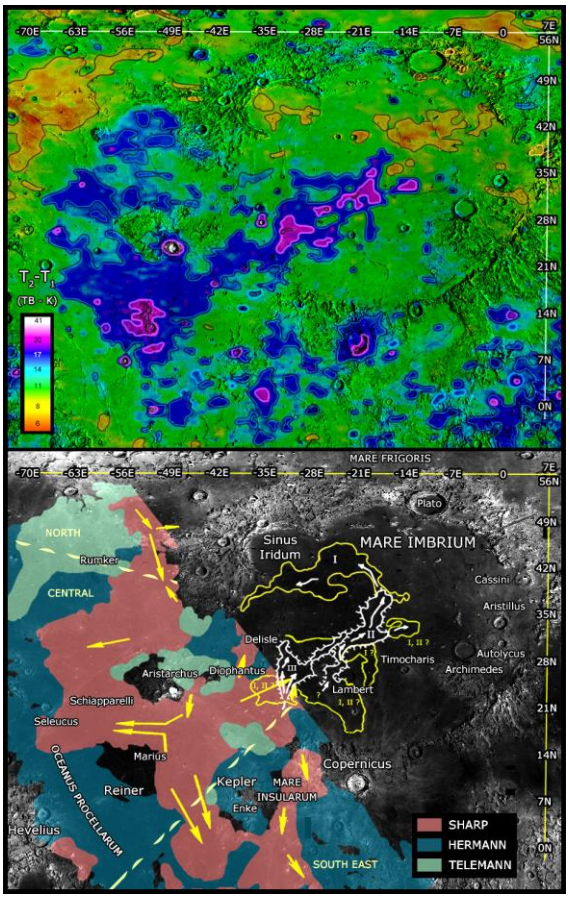

Figure 1. Upper. Map shows the temperature differences (K) at midnight between the temperature average of the surface layer down [8] expressed as 'Brightness Temperature' (TB); below: 1] distribution of three formations in Mare Procellarum as described by [9] based on UV/VIS ratio, albedo, and other parameters. Arrows show proposed flow directions of units the for Sharp formation; Lower. Proposed areal distribution of the three most recent mare flows within the Imbrium basin (I-III), according to [10]. Background image is a lunar Clementine Global UVVIS 750 nm mosaic [11] overlaid on a shaded relief map [12].

EPSC Abstracts
Vol. 12, EPSC2018-735, 2018
European Planetary Science Congress 2018
© Author(s) 2018

Nature of cone distribution at aureole of Olympus Mons, Mars

R. Parekh and A. Shukla
Geoscience division, Physical Research Laboratory, Ahmedabad, India (rutu@prl.res.in, adshukla@prl.res.in)

Abstract

Olympus Mons is suspected as a site of latest volcanic activity on Mars and various theories have been suggested for the origin of deposit surrounding the main dome. The analysis of cone is expected to enhance our knowledge with regard to the origin of deposit and the region condition. In our study, we analysed distribution and variation in size of aureole cones by using high resolution CTX and HiRISE images along with topographic information.

1. Introduction

The analysis of large cone fields may provide new line of evidence to understand relationship between climate, volcanism and hydrothermal systems on Mars [7].

For our study purpose we have chosen the north region of Olympus Mons known as aureole deposit (Lat: 30° N to 36° N, Long: 133°W to 140° W). The shield volcano, Olympus Mons is one of the largest volcanoes in the Solar System [5]. The volcano consists of main dome with calderas at the top. The aureole deposit is widespread from the bottom of dome and makes groove terrain that can be easily differentiate. The entire region is believed to contain water and lava in past [7]. In fact, the presence of lava floods and water/ ice has been proposed on the surface of Mars [2, 11]. The source of water or lava floods is not clear yet, but it generated relatively young smooth surface (probably mid to late Amazonian period) on Mars [7, 8] by resurfacing process. The smooth plain is characterised by some of the distinct targets, one of them is large cone fields.

In the current study, we identified and analysed cone structure on the north of Olympus Mons aureole. The cone fields are easily distinguished due to their bright steep slope and high elevation. Similar cone structures are present in Iceland on Earth [4, 9]. The Iceland cones resemble the cones which are observed on Mars [3, 6]. By taking these cones as a reference, we can identify the cone group on Mars. The cones form due to the explosive interaction between lava and water which may be in the form of liquid or solid [1]. The identified cones depict a large variety of morphologies and sizes.

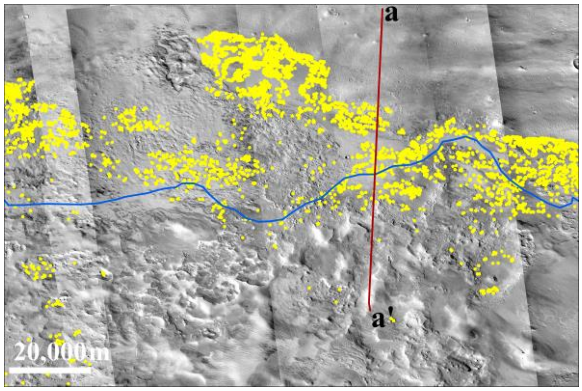

Figure 1 Red dots indicates identifies location of cones in CTX and HiRISE. Maroon (a- a'): is a counting line for cone, perpendicular to the basin. Blue line: primary flow line. North up.

2. Methodology

Our aim is to analyse the distribution patter, size and morphology of cones and understand possible formation mechanism for the observed features. For detail distribution pattern analysis we counted number of cones along the line (a-a', Fig. 1), parallel to flow line (blue line in Fig. 1) and divided the region into 1.7 km^2 boxes each (counting method adopted from Noguchi & Kurita, 2015).

3. Observations

The cones of aureole follows unique distribution pattern: large number of cones is concentrated on the flanks of the flow channel (Fig. 2B) and parallel to the flow direction. The cones concentrated at the flank are dominantly of small in size (<300m, Fig. 2C) where as large cones (>300m, (Fig. 2C) are confined in the center part of the valley in aureole. Similar phenomena is seen in case of Athabasca valley, where double cones and lotus cones are confined at the central part of the channel in low elevated area [10].

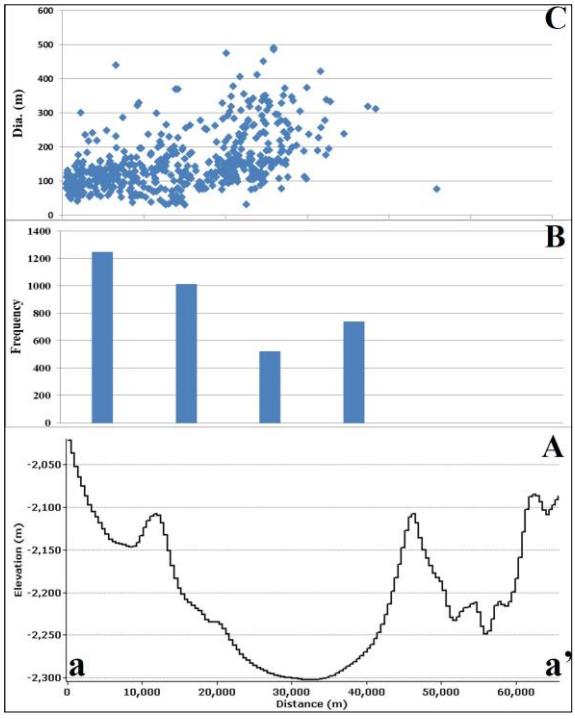

Figure 2 (A) Elevation graph of basin perpendicular to the primary flow (a-a')(B)Distribution graph of cone perpendicular to the flow direction. Large number of cone group is clustered at the flank of the basin. The topographic information taken from MOLA MEGDR (NASA/Cal-Tech/ASU). (C)Distribution of cones according to its crater size.

The large spectrum of variation in cones depends upon the availability of resources (water and/or lava) during the time of formation [10]. In case of Asthabasca Valley, the thick lava flow in the central part channel and large amount of water/ ice in the pore space are thought to be one of the reason for large double cones and lotus cones [10]. We are assuming similar mechanism could be the reason for larger cone size in our stud region.

Furthermore, DEM from HiRISE stereo pairs will be generated to study detail cone morphology and measurement of slope, height of cones.

References

[1]Bleacher et al., 2009, Jour. of Volca. and Geothe. Research, 185(1–2), 96–102.

[2] Bleacher et al., 2007, JGR: Planets, 112(4), 1–10.

[3]Brož and Hauber, 2012, Icarus, 218(1), 88–99.

[4]Bruno et al., 2006,JGR: Planets, 111(6).

[5]Carr and Head, 2010, Elsevier B.V.

[6]Hamilton et al., 2011, JGR: Planets, 116(3).

[7]Head et al., 2005, Nature, 434(7031), 346–351.

[8]Keszthelyi et al., 2010, Icarus, 205(1), 211–229.

[9]Noguchi et al., 2017, Epsc, 11, 3–4.

[10]Noguchi and Kurita, 2015, PSS, 111, 44–54.

[11]Plescia, J. B, 2003, Icarus, 164(1), 79–95.

EPSC Abstracts
Vol. 12, EPSC2018-739-1, 2018
European Planetary Science Congress 2018
© Author(s) 2018

Mapping of regional C-C'-S shear zones on the floor of Valles Marineris troughs

Daniel Mège and Joanna Gurgurewicz
Space Research Centre PAS, Poland (dmege@cbk.waw.pl, jgur@cbk.waw.pl)

Abstract

The floor of Hebes Chasma and Ophir Chasma, the two elliptical and deepest troughs of Valles Marineris, displays NE-SW to ENE-WSW several kilometres wide dextral brittle-plastic shear zones. Structural maps of these areas are presented. Mapping suggests that the northern part of Valles Marineris is probably composed of large sheared tectonic blocks that moved relative to each other while Valles Marineris was being stretched perpendicular to its main, ESE trend. The block boundaries played a role in guiding the further tectonic and geomorphologic evolution of Valles Marineris.

1. Introduction

The formation mechanisms of the large northern troughs of Valles Marineris, especially Ophir Chasma and Hebes Chasma, has remained poorly understood because of the lack of obvious tectonic structures that would have guided floor subsidence. On the one hand, tectonics was probably involved because we do see narrow grabens parallel to these troughs being cut by the troughs, and dykes exposed on the floor of Ophir Chasma. On the other hand, floor erosion must have been intense too in order for deep exposures of these dykes to be visible today [1], severely restricting the role of tectonic subsidence. We present structural maps based on interpretation of HiRISE imagery that provide further constraints on the role of tectonics, but also erosion, in the formation of these troughs. The maps demonstrate the existence of huge brittle-plastic shear zones in Ophir Chasma and Hebes Chasma, the implications of which for the formation and evolution of Valles Marineris are discussed.

2. Shear zones

HiRISE images reveal shear zones in the deepest parts of Hebes and Ophir chasmata (Figure 1) that were active before the ILDs were deposited. The sheared rocks are unstratified. Some occurrences have been interpreted as sulfate-rich, based on CRISM data [2], and have similar brightness and morphology as sulfate-rich deposits that precipitated during the opening of Valles Marineris in Ius Chasma [3]. Nevertheless, some outcrop geometric patterns are reminiscent of plutonic bodies. Dykes of thickness up to tens of metres are also observed. The shear zones display brittle-plastic structural fabrics, which on Earth are found in mylonite zones. They include S/C, S/C', as well as a combination of C, C' and S-type shears. The geometry of the S-type shears points to overall dextral shear zone kinematics.

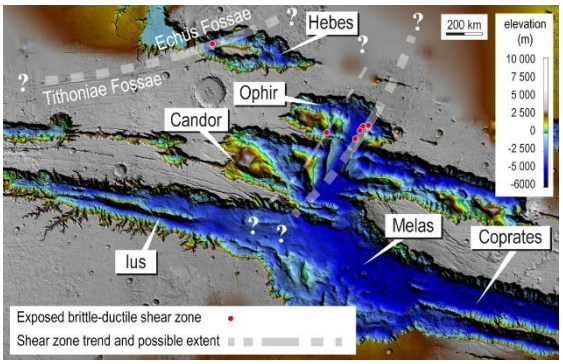

Location of the main shear zone exposures and extrapolated trends. The base map is the HRSC digital elevation model of Valles Marineris.

The Ophir Chasma shear zones are located in eastern Ophir, along the corridor that connects Ophir Chasma and Candor Chasma, and in southwest Ophir (Figure 1). The NE-SW orientation of the C-type shears matches the general orientation of the corridor. The most complex shear zone geometry is found in eastern Ophir, with an association of well-developed dextral C-type and C'-type shears, each associated with their own S-type shears. A more detailed account of this shear zone is provided in [4]. In western Ophir, the identified shear zone is less well exposed but its orientation and kinematic appear similar.

The Hebes Chasma shear zone is geometrically more

simple than those observed in Ophir Chasma, with textbook successions of C-type shears and associated S-type shears. It is approximately parallel to, and perhaps connects, ENE-oriented narrow grabens of Tithoniae Fossae and the southeasternmost grabens of Echus Fossae.

3. Implications

Shear zone width is difficult to ascertain due to the sedimentary cover on the chasma floor, such as the ILDs, landslide deposits, dunes, and moraines. Nevertheless, the same shear system is crossed over more than 3 km perpendicular to strike in eastern Ophir Chasma, and 8 km in Hebes Chasma. Such widths are on Earth correlated with shear zone horizontal displacements one order larger, i.e. tens of kilometres [5], probably implying total shear zone length of one to several thousands of kilometres (e.g., [6]).

Because of the alignment between one of the shear zones and the Ophir-Candor corridor, and the consistency between shear zone kinematics and normal faulting parallel to the main Valles Marineris troughs, it may be reasonably proposed that while being stretched, the Valles Marineris crust was undergoing dextral shearing that decoupled the eastern from the western portions of Valles Marineris along a line going through Ophir Chasma and Candor Chasma. C'-type shears preferably form in extensional tectonic context on Earth [7], supporting simultaneity of strike-slip faulting along the Ophir-Candor corridor and normal faulting of the whole Valles Marineris tectonic system (e.g., [8]). The shear zone located along the Ophir-Candor corridor would then be akin to transfer faults on terrestrial continental rift zones, which in general are inherited structures (e.g., [9]).

Alignment of the Hebes Chasma shear zone with the Tithoniae and Echus narrow grabens, the kinematics of which appears to be purely tensional after the latest lava outpourings, suggests that the shear zone was reactivated in tension during or after the Early Hesperian [10].

If formed in pure tensile mode, the kinematics along the identified dykes are not always consistent with the shear zone kinematics inferred from the S/C and S/C' fabrics. In Hebes Chasma, the stress regime that would be appropriate to dyke propagation would imply sinistral shearing. Such dykes, of orientation close to N-S, have been identified elsewhere in Valles Marineris as well [11]. No evidence has been found, however, that the dykes themselves are deformed by the shears; they might testify to post-shear E-W extension.

4. Conclusions

Structural mapping reveals huge brittle-plastic shear zones that affect the deepest parts of Hebes Chasma and Ophir Chasma. Similar deformation has been sought in other chasmata unsuccessfully, at least because of the widespread sedimentary cover. These shear zones, exposed after removal of kilometres of crust, are an important element of the evolution of Valles Marineris, for instance by delimiting large tectonic blocks during Valles Marineris formation, mechanically decoupling its eastern and western parts, and probably guiding the erosional corridor between the Ophir and Candor troughs.

Acknowledgements

This work was funded by the OPUS/V-MACS project no. 2015/17/B/ST10/03426 of the National Science Centre, Poland.

References

[1] Mège, D. and Gurgurewicz, J.: The Ophir Chasma Dyke Swarm: description and implications for the genesis of the Valles Marineris northern troughs, Acta Geol. Sin.-Engl., Vol. 90, pp. 180-182, 2016. [2] Wendt, L. et al.: Sulfates and iron oxides in Ophir Chasma, Mars, based on OMEGA and CRISM observations. Icarus, Vol. 213, pp. 86-103, 2011. [3] Roach, L.H., et al.: Hydrated mineral stratigraphy in Ius Chasma, Valles Marineris. Icarus, Vol. 206, pp. 253–268, 2010. [4] Gurgurewicz, J., and Mège, D.: Deep tectonics exposed in northern Valles Marineris, Mars, EPSC Abstracts, Vol. 12, EPSC2018-430, 2018. [5] Fossen, H.: Structural geology, Cambridge Univ. Press, 2016. [6] Schultz, R.A., et al.: Displacement-length scaling relations for faults on the terrestrial planets, J. Struct. Geol., Vol. 28, pp. 2182-2193, 2006. [7] Passchier, C.W.: Geometric constraints on the development of shear bands in rocks, Geol. Mijnbouw, Vol. 70, pp. 203-211, 1991. [8] Mège, D. and Masson, P.: A plume tectonics model for the Tharsis province, Mars, Planet. Space Sci., Vol. 44, pp. 1499-1546, 1996. [9] Bellahsen, N., et al.: Pre-existing oblique transfer zones and transfer/transform relationships in continental margins, Tectonophysics, Vol. 607, pp. 32-50. [10] Tanaka, K.L., et al.: Geologic map of Mars: U.S. Geological Survey Scientific Investigations Map 3292, 2014. [11] Mège, D. and Gurgurewicz, J.: On Mars, location and orientation of dykes exposed along the Valles Marineris walls reveal expected and unexpected stress fields, Acta Geol. Sin.-Engl., Vol. 90, pp. 177-179, 2016.

EPSC Abstracts
Vol. 12, EPSC2018-852, 2018
European Planetary Science Congress 2018
© Author(s) 2018

Spectral properties of pyroclastic deposits on Mercury and the Moon

Besse Sebastien (1), Alain Doressoundiram (2) Oceane Barraud (2) Thomas Cornet (1) and Claudio Munoz (2)
(1) European Space Agency, ESAC, Madrid, Spain (2) LESIA, Observatoire de Paris, Meudon, France
(sbesse@sciops.esa.int)

Abstract

Explosive volcanism is a process commonly present on the surface of the Moon and Mercury. Instrumentation with similar capabilities onboard spacecraft orbiting both planetary objects can allow cross comparison of similar processes in different contexts. Our analyses show that similar spectral characteristics are observable on these objects, which might emphasize that similar processes drive and form pyroclastic deposits on the Moon and Mercury.

1. Introduction

Volcanism exposed on the surface of planets is a unique opportunity to get insights about its interior, and Mercury is no exception with the confirmation of widespread volcanism on the surface [1,2,3]. In addition, the surprising high concentration in volatile elements [4], and the poor concentration in iron of its surface with respect to its supposedly large iron-rich core are highlighting the complex history of Mercury. On the Moon, Pyroclastics Deposits (PDs), markers of explosive volcanism, have been identified since a very long time and numerous authors have characterised their location and properties [5], although new insights have been recently obtained with new instruments orbiting the Moon [6, 7, 8].

2. Mercury's pyroclastic deposits

While Kerber et al. [3] have shown that PDs on Mercury are spectrally flat and similar in albedo to those on the Moon, Goudge et al. [9] highlighted the ultraviolet (UV) and visible (VIS) characteristics of 35 PDs. Besse et al. [10] detailed analysis of Caloris' PDs have confirmed the UV and VIS properties of the PDs, and also added that PDs are distinguishable in the near-infrared (NIR) domain with respect to Mercury's surface spectral average properties. Besse et al. [10] also demonstrated that similarly to the Moon [6], spectral properties of PDs of the Caloris basin change as a function of distance to the source.

3. Lunar pyroclastic deposits

The extended analysis of Gaddis et al. [5] has set the benchmark for spectral analysis of lunar deposits. Only new instruments such as Moon Mineralogy Mapper and the lunar Reconnaissance Orbiter Camera can help discovering new PDs and their characteristics. Although observed at the surface of the Moon, Besse et al. [7] found direct association between volcanic glass and explosive volcanism in numerous cases. While Jawin et al. [6] investigated new PDs, a direct relationship between the spectral properties and the distance to the source has been clearly identified, as it has been shown in the case of Mercury [10].

4. Lunar and Hermean Pyroclastic deposits are not that different

Separate spectral analysis using different instruments orbiting Mercury and the Moon is highlighting similar properties and behavior that could indicate similar processes generating explosive volcanism. Of particular interest is the variability of the spectral parameters as a function of distance that is clearly being observed on both objects. Although the lunar variability is easily associated to composition (and a decrease in mafic material), the conclusion is much more complicated for Mercury given the lack of information on composition. In any case, detailed analysis on Mercury and the Moon provide details on the mechanisms that generate pyroclastic deposits and their numerous commonalities.

During the conference, we will present our state of the art analysis on pyroclastic deposits, and our ideas on the common processes that might occur on the Moon and Mercury.

References

[1] Head, J. et al.,: Flood Volcanism in the Northern High Latitude of Mercury Revealed by MESSENGER, Science, 2011.

[2] Prockter, L. et al.: Evidence for Young Volcanism on Mercury from the Third MESSENGER Flyby, Science, 2010.

[3] Kerber, L. et al.,: Global Distribution of pyroclastic deposits on Mercury: The view from MESSENGER flybys 1-3, Planetary and Space Science, 2011.

[4] Nittler, L. et al.,: The Major-Element Composition of Mercury's Surface from MESSENGER X-ray spectrometry, Science, 2011.

[5] Gaddis, L. et al,.: Compositional analysis of lunar pyroclastic deposits, Journal of Geophysical Research, 2003.

[6] Jawin, E. et al.,: Examining spectral variations in localized lunar dark mantle deposits, Journal of Geophysical Research, 2015.

[7] Besse, S. et al.,: Volcanic glass signatures in spectroscopic survey of newly proposed lunar pyroclastic deposits, Journal of Geophysical Research, 2014.

[8] Gustafson, O. et al.,: Characterization of previously unidentified pyroclastic deposits using Lunar Reconnaissance Orbiter Camera data, Journal of Geophysical Research, 2012

[9] Goudge, T. et al.,: Global inventory and characterization of pyroclastic deposits on Mercury: New insights into pyroclastic avtivity from MESSENGER orbital data, Journal of Geophysical Research, 2014.

[10] Besse, S. et al.,: Spectroscopic properties of explosive volcanism within the Caloris basin with MESSENGER observations, Journal of Geophysical Research, 2003.

EPSC Abstracts
Vol. 12, EPSC2018-884, 2018
European Planetary Science Congress 2018
© Author(s) 2018

The impact of data resolution and magmatic resurfacing events on understanding fault growth behaviour in the volcanic regions of Iceland and Mars

Emma Bramham, Douglas Paton
Institute of Applied Geosciences, School of Earth and Environment, University of Leeds, UK (E.K.Bramham@leeds.ac.uk)

Abstract

We show a comparative study of fault behaviour in the volcanic regions of Krafla, Iceland and Alba Patera, Mars. The study highlights the importance of both data resolution and magmatic resurfacing in controlling any comparison between fault behaviour in potentially analogous regions both on a single planet and across the Solar system.

1. Introduction

Despite differences in the tectonic settings on Mars and Earth, comparative studies of normal faulting behaviour on these two planets could be one of the routes to understanding parameters, such as surface gravity and lithospheric strength, which control variations in crustal processes across planetary bodies [1]. Comparisons can be made between the distribution of Terran maximum displacement/length (D_{max}/L) relationship of faults and those measured on Mars [7]. However, usefully extracting values controlling differences in fault growth behaviour relies not only on being able to constrain the effects of differences in data resolution but also in understanding variations in tectonic settings on Earth. In this study we have compared D_{max}/L measurements made at a range of resolutions on Earth at the actively rifting, Krafla volcanic zone, NE Iceland [2,5] and on Mars in the region of fault systems in the northern region of Alba Patera [3,6,7].

2. Method

For the Krafla faults, we created a 0.5 m resolution digital elevation model (DEM) of the area from airborne LiDAR, additionally downsampling to create 10 m and 30 m DEMs. From these we measured three major fault systems, as single faults at 30 m resolution, and all component faults at 10 m and 0.5 m resolution. For the Martian faults we measured fault systems as single faults using ~460 m resolution Mars Orbiter Laser Altimeter (MOLA) data and as component faults using ~6 m resolution Context Camera (CTX) stereographic image data from the Mars Reconnaissance Orbiter (MRO). Examples are shown in figure 1.

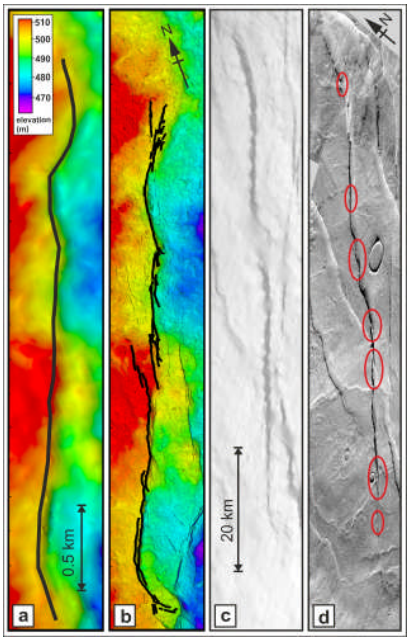

Figure 1. Showing a single fault system in Krafla (a) and Alba Patera (b), using 30 m resolution LiDAR and 360 m resolution MOLA data respectively. The corresponding segmented faults shown using 0.5 m resolution LiDAR and 6 m resolution CTX data.

To allow comparative measures between the magmatically resurfaced regions of Alba Patera and similar regions on Earth, we used the 0.5 m resolution to measure the displacement/length profiles of 775 faults in a magmatically resurfaced area of Krafla to develop a model of fault growth through resurfaced layers, with lengths ranging from 10s to 1000s of metres.

3. Results

The D_{max}/L data for an example fault system from Krafla and Alba Patera are shown in figure 2 (a and b respectively). For the Krafla data, all fault systems measured shown a similar distribution, with single faults in low resolution showing a low D_{max}/L and a spread of segmented faults in the high resolution data that sit at the top end of the Terran D_{max}/L distribution. A similar result can be seen with the Martian fault data when compared with the published Martian distribution. Additionally, the high resolution data is observed to be within the Terran published distribution.

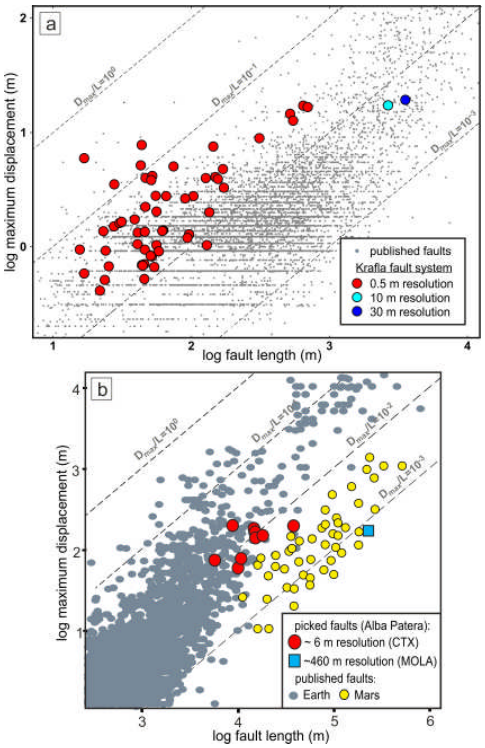

Figure 2. Example Dmax/L data for a single (a) Krafla and (b) Alba Patera fault system. Published fault data: Terran (grey) as shown in [1], and Martian (yellow), as shown in [7]

4. Summary and Conclusions

Potential limitations in understanding fault segmentation and the effectiveness of direct comparison of fault behaviour, both between locations on Earth and between fault populations on different planets and moons, can be controlled by the resolution of the data being used. Additionally, we observe that, in a magmatically resurfaced region, continued fault growth may result in a lower D_{max} across the fault system (measured as a single fault in low resolution data) as the fault re-establishes through a segmented system of faults at the surface. In attempting to understand and quantify parameters that act as key controls to differences in behaviour across planetary bodies, influences such as varying data resolution and magmatic resurfacing must be considered.

Acknowledgements

To NERC ARSF for the LiDAR data acquisition and to NCEO and COMET+ for funding the Icelandic research. To NASA for providing MOLA and CTX data and the ASP software (NASA) and USGS-ISIS software used for processing CTX images.

References

[1] Bailey, W., J. Walsh, and T. Manzocchi: Fault populations, strain distribution and basement fault reactivation in the East Pennines Coalfield, UK, Journal of Structural Geology, 27 (5), 913-928, 2005

[2] Bramham, E.., Paton, D., Wright, T.: How Segmented is your fault? Deciphering fault relationships from low resolution data, EGU General Assembly Conference Abstracts 19, 15205, 2017

[3] Hauber, E., Grott, M., Kronberg, P.: Martian rifts: Structural geology and geophysics, Earth and Planetary Science Letters, 294, 393-410, 2010

[4] Heap, M.J., Byrne, P.K., Mikhail, S.: Low surface gravitational acceleration of Mars results in a thick and weak lithosphere: Implications for topography, volcanism, and hydrology

[5] Hjartardottir, A.R., Einarsson P., Bramham, E., Wright, T.J.: The Krafla fissure swarm, Iceland, and its formation by rifting events

[6] Öhman, T., McGovern, P.: Circumferential graben and the structural evolution of Alba Mons, Mars, Icarus, 233, 114-125, 2014

[7] Schulz, R.A., Okubo, C.H., Wilkins, S.J.: Displacement-length scaling relations for faults on the terrestrial planets, Journal of Structural Geology, 28 (12), 2182-2193, 2006

EPSC Abstracts
Vol. 12, EPSC2018-968, 2018
European Planetary Science Congress 2018
© Author(s) 2018

Hf/W insights into the primeval Moon

Maxwell M. Thiemens (1), Peter Sprung (1), Raúl O.C. Fonseca (1), Felipe P. Leitzke (2) and Carsten Münker (1)
(1) Institute für Mineralogie und Geologie, Universität zu Köln, Germany, (2)Steinmann Institute, University of Bonn, Germany (m.thiemens(at)uni-koeln.de)

Abstract

The Moon formed in the aftermath of a giant impact of a planetesimal into the growing proto-Earth. The timing of this event is a key event in the early history of our Solar System and Earth. Age estimates for lunar formation are subject to ongoing debate. These ages estimates vary between those who believe in an "old Moon," (which formed between 30 and 70 Myrs after solar system formation) and those who believe in a young Moon (from ca. 80 to 200 Myrs after solar system formation). The Moon bears an excess in ^{182}W compared to the Earth, and grasping the nature of this excess is a key step towards a more profound understanding of the Earth-Moon system. We present high-precision isotope dilution measurements of relevant trace elements for a wide range of lunar samples, with an emphasis on High Field Strength Elements (HFSE). By coupling these with recent HFSE crystal/silicate melt partitioning data relevant to lunar magmatism, we find that the lunar mantle bears a resolvably higher Hf/W ratio than the bulk silicate Earth. We can therefore explain the ^{182}W excess observed in lunar samples as the result of the radiogenic ingrowth of ^{182}W that resulted from the decay of the still extant ^{182}Hf, implying that the Moon must have formed while the Hf-W decay system was extant.

1. Introduction

Lunar rocks provide a snapshot of the early solar system, and insights into the processes involved during planetary formation and differentiation. These processes require an understanding of the differentiation events of the Moon, such as core formation, the crystallization of the Lunar Magma Ocean (LMO), and generation of lunar mare basalts. This understanding is best achieved by combining observations and data obtained from natural samples, with data from experimental studies dealing with lunar magmatism. We pursue this by exploring redox-sensitive trace element behavior during lunar magmatism and modeling its implications for Hf-W chronometry. Tungsten and U, for example, are regarded as behaving geochemically identical during partial melting in the Earth's upper mantle. However, mineral/melt experimental partitioning data have shown that U and W are less incompatible at more reduced fO_2 conditions, such as those prevalent during lunar mantle melting [1,2]. The higher mineral/melt partition coefficient of W^{4+} relative to W^{6+} will significantly affect the overall compatibility of W in lunar mantle residual phases during partial melting. This, in turn, will fractionate W from U and other High Field Strength Elements (HFSE). Therefore, we combined whole-rock high-precision HFSE and Hf-Nd isotope data in lunar samples with core formation, crystallization, and aggregate fractional melting models to better understand the petrogenesis of major lunar rock types and quantify the lunar W budget with implications for the ^{182}W systematics of the Earth and the Moon.

2. Methods

Lunar samples were obtained from the Curation and Analysis Planning Team for Extraterrestrial Materials (CAPTEM), including 7 high-Ti mare basalts and soils, 14 low-Ti mare basalts, 2 ferroan anorthosites (FANs), and 7 KREEP-rich samples. Mixed HFSE and U-Th isotope tracers were added prior to digestion. The elements of interest were isolated for analysis on the University of Cologne's MC-ICP-MS following the methods of [4]. External precision and accuracy for elemental ratios determined by isotope dilution are typically better than ±1% for U/W and Th/W (2σ r.s.d.). Typical blanks during the course of the measurements were better than 50 pg for W, 60 pg for U, 30 pg for Th, and 30 pg for Hf. These blanks proved negligible, with blank uncertainty derived propagated errors less than ±1%. Our Lunar Magma Ocean fractionation model was created based on a cumulate crystallization sequence [3]. To define the starting composition for the silicate Moon we modeled the geochemical constraints for the variation of major- and trace-element and Nd, Sr, and Hf isotope features of the lunar sample suite reported in the literature [4,5]. For W, an additional mass balance between the estimate of its content in the

bulk silicate Moon after core formation was performed [6], considering different core mass fractions (1-3% of the total mass of the Moon). Trace element crystal/silicate melt partition coefficients for pyroxene, plagioclase, and olivine were selected considering the variation of TiO_2 exhibited by lunar mare basalts [2] and the effect of fO_2 on the behavior of W [1,2]. Ilmenite/silicate melt trace element partition coefficients are an average of the high-Ti experiments listed described by [7].

3. Results and Discussion

Our data for low-Ti mare basalts U/W range between 1.6 to 2.6 and Hf/W between 30 to 50. Within individual groups the low-Ti basalts are fairly uniform (U/W generally varies by 0.1, Hf/W by ca. 5). Amongst the high-Ti mare basalts, the Apollo 17 samples show variable Hf/W up to 150 and correlated U/W up to 2.3, clearly distinct from the A11 high-Ti basalts (Hf/W of 40 to 60 and U/W between 1.5 and 2.2) and all low-Ti basalts. Similarly, most samples show Zr/Nb between 14 and 18 while A17 high-Ti mare basalts fall below 10. Melting models (continuous & fractional melting, ± residual metal) and the within-group homogeneity of low-Ti mare basalts imply that the source compositions per group are virtually identical but differ from group to group. This agrees with the distinct Hf-Nd isotopic and extended HFSE features found amongst different groups of low-Ti mare basalts, which require similarly distinct mantle sources [4,5]. A unique A17 high-Ti mantle source implied by Hf-Nd isotopes [5] is compatible with variable Hf/W and correlated U/W of A17 basalts given the likely presence of residual Fe-Ti oxides and metal at the source [1,2]. Across our samples, we find a uniformly elevated Hf/W in the lunar samples, corroborating previous studies [e.g. 10].

The assumption that W is less incompatible than Hf during the formation of LMO cumulates, which became the source of lunar mare basalts [1,2,5], requires a re-evaluation of the Hf/W of the lunar mantle. The mineral constituents of the low-Ti mantle sources preferentially retain W over Hf and U during LMO crystallization at the low lunar fO_2. Therefore, the measured Hf/W of low-Ti lunar mantle sources define minimum estimates of the Hf/W in the sources and, by inference, of the bulk LMO as well as of the silicate Moon. When modeling source compositions from the measured samples, it can be inferred that the Hf7W of the bulk silicate Moon is higher than that of the bulks silicate Earth, at least by 20-30%.

There are three broad scenarios that can account for the elevated Hf/W of the Moon. The first scenario holds that a late veneer of material with a Hf/W of ~1 lowers the Hf/W of the Earth-Moon system. As the Earth is struck by a proportionally larger amount of material, the bulk silicate Earth's ratio is lowered to 25.6, while the Moon retains a uniformly higher Hf/W closer to the original Hf/W of the system. The second explanation holds that the Moon forming event occurs while ^{182}Hf is extant, and the Earth's Hf/W is lowered following lunar formation by ongoing core formation and increasingly oxidized conditions on the Earth. The final explanation holds that the Moon forms while ^{182}Hf is extant, and the formation of the lunar core elevates the silicate Moon's Hf/W signature.

4. Acknowledgements

MMT and CM acknowledge funding from ERC grant 669666 "Infant Earth"; ROCF acknowledges funding for a Heisenberg Fellowship by the Deutsches Forschungsgemeinschaft through grant DFG FO-693-5-1; F.P.L. acknowledges funding by the DAAD/CNPq (248562/2013-4). PS acknowledges funding from UoC emerging fields grant "ULDETIS." Partial funding for MMT from DFG grant SP 1385/1-1.

5. References

[1] Fonseca et al. (2014) *Earth Planet. Sci. Lett*. 404, 1–13 [2] Leitzke et al. (2016) *Chem.Geol*. 440, 219–238 [3] Snyder et al. (1992) *Geochim. Cosmochim. Acta* 56 (10), 3809–3823 [4] Münker, C. (2010) *Geochim. Cosmochim. Acta* 74, 7340-7361 [5] Sprung et al. (2013) *Earth Planet. Sci. Lett.* 380, 77-87 [6] Steenstra et al. (2016). *Earth Planet. Sci. Lett.* 441, 1–9. [7] Dygert et al. (2013). *Geochim. Cosmochim. Acta* 106, 134–151 (2013). [8] Kleine et al. (2002) *Nature* 418, 952-955. [9] König et al. (2011) *Geochim. Cosmochim. Acta* 75 (8), 2119–2136. [10] Kruijer et al. (2015) *Nature* 520, 534-537 [11] Touboul et al., (2015) *Nature* 520, 530-533

EPSC Abstracts
Vol. 12, EPSC2018-1161, 2018
European Planetary Science Congress 2018
© Author(s) 2018

Extensive Volcanic Resurfacing within the South Pole – Aitken Basin

Daniel P. Moriarty III and N. E. Petro
NASA Goddard Space Flight Center, Greenbelt, Maryland, USA
Daniel.p.moriarty@nasa.go

1. Introduction

The South Pole - Aitken Basin (SPA) is a vast, ancient impact structure on the lunar farside. Understanding SPA is central to several critical lunar science questions relevant to (1)basin chronology, (2)lower crust/upper mantle stratigraphy and composition, (3)large impact processes, (4)lunar formation/thermal evolution, and (5)lunar volcanism. Recently, we used Moon Mineralogy Mapper (M3) data to evaluate the compositional structure of the basin, identifying four distinct compositional zones [1]. The center-most zone, the SPA Compositional Anomaly (SPACA), exhibits several lines of evidence for extensive volcanic resurfacing.

2. Volcanic Resurfacing Across SPACA

Moriarty and Pieters [1] note several lines of evidence for volcanic resurfacing, across the SPACA region. From local stratigraphy at impact craters within SPACA, the zone was inferred to have a several km thick layer of Ca,Fe-bearing pyroxenes overlying a Mg-pyroxene-rich unit. The SPACA region also exhibits a relatively smooth morphology, with a low density of impact craters. A large proportion of the craters present show signs of significant modification through embayment, burial, or flooding. These pieces of evidence point to extensive resurfacing. But what is the nature of this resurfacing deposit? Do these materials represent an unusual extrusive magma composition? Well-mixed ejecta from nearby basins? A long-lived, differentiated impact melt sheet? Extensive, well-mixed cryptomare? The relationship of SPACA surface materials to the enigmatic structure known as Mafic Mound [2], may provide clues. Mafic Mound is a ~70 km local topographic high within SPACA that has been interpreted to be a volcanic construct based on its morphology and unusual mineralogy. Since the composition of SPACA surface materials are similar to Mafic Mound, this implies a similar formation mechanism. This strongly suggests a volcanic origin for the extensive resurfacing observed within SPACA Understanding SPACA is key for unraveling the complex geologic, geophysical, and thermal evolution of South Pole - Aitken.

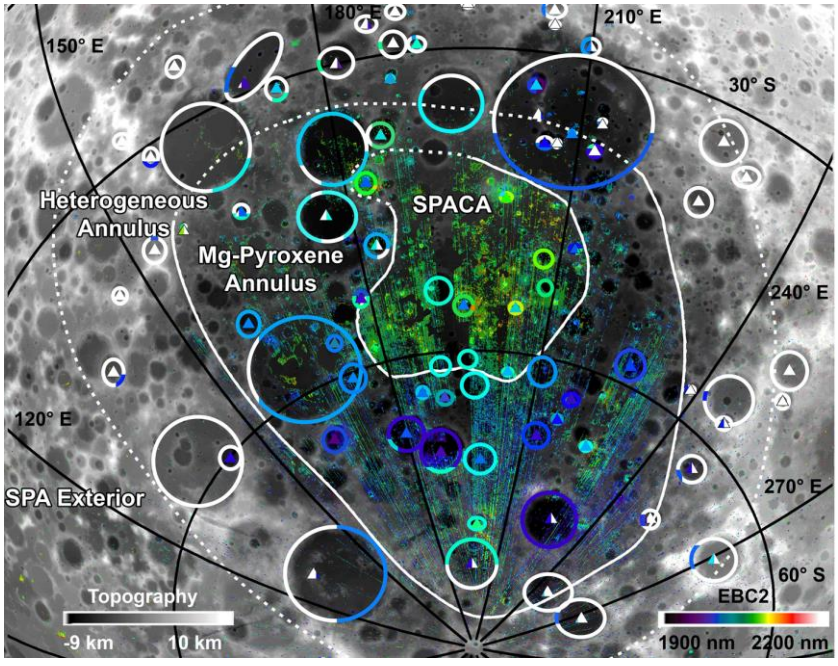

Figure 1: The four distinct compositional zones of SPA as defined in [1]. Basemap is LOLA topography. Colorized pixels correspond to the band center of the 2 micron absorption band derived from M3 data. These band centers are sensitive to pyroxene composition. In general, short wavelength bands correspond to Mg-rich pyroxenes, while longer

wavelength bands correspond to more Ca,Fe-rich pyroxenes. Superposed symbols represent the dominant pyroxene compositions of a suite of large impact structures studied, based on absorption band center. White symbols indicate feldspathic compositions. Known mare basalts have been masked from the M3 pixels to emphasize the diversity in SPA basin materials.

Acknowledgements

We would like to thank Carle Pieters and Jim Head for helpful discussions in developing this research. The authors are grateful to the NASA Postdoctoral Program for funding this research and travel to EPSC.

References

[1] Moriarty, D. P., & Pieters, C. M. (2018). The Character of South Pole‐Aitken Basin: Patterns of Surface and Subsurface Composition. Journal of Geophysical Research: Planets, 123(3), 729-747.

[2] Moriarty, D. P., & Pieters, C. M. (2015). The nature and origin of Mafic Mound in the South Pole‐Aitken Basin. Geophysical Research Letters, 42(19), 7907-7915.